

Experimental analysis on the effect of local base blowing on three-dimensional wake modes

M. Lorite-Díez¹, J. I. Jiménez-González^{1†}, L. Pastur², C. Martínez-Bazán¹ and O. Cadot³

¹Departamento de Ingeniería Mecánica y Minera. Universidad de Jaén. Campus de las Lagunillas, 23071, Jaén, Spain.

²IMSIA-ENSTA ParisTech, 828 Bd des Maréchaux F-91762 Palaiseau, France.

³School of Engineering, University of Liverpool, Liverpool L69 3GH, UK.

(Received xx; revised xx; accepted xx)

Wake modes of a three-dimensional blunt-based body near a wall are investigated at a Reynolds number $Re = 10^5$. The targeted modes are the static symmetry breaking mode and 2 antisymmetric periodic modes. The static mode orientation is aligned with the horizontal major y -axis of the base and randomly switches between a positive P and a negative N state leading to long-time bistable dynamics of the turbulent wake. The 2 periodic modes have Strouhal numbers for oscillations aligned respectively with the major y -axis and minor z -axis of the base. The modifications of these modes are studied when continuous blowing is applied at different locations through 4 slits along the base edges (denoted L for left, R for right, T for top and B for bottom) in either 4 single asymmetric configurations or 2 double symmetric configurations (denoted LR and TB). Two regimes, referred to as mass and momentum are clearly identifiable for all configurations. The mass regime, which is poorly sensitive to blowing momentum and location, is characterized by the growth of the recirculating bubble as the total injected flow rate is increased, being it associated with a base drag reduction and interpreted as resulting from the equilibrium between mass fluxes feeding and emptying the recirculating region as introduced by Gerrard (1966) for two-dimensional bodies. A simple budget model is shown to be in agreement with entrainment velocities measured for isolated turbulent mixing layers. The strength of the static mode is reduced up to 20% when the bubble length is maximum, whereas no change in the periodic mode frequencies is found. Besides, the momentum regime is characterized by the deflating of the recirculating bubble leading to base drag increase. It is interpreted by the free shear layers forcing which increases the entrainment velocity thus emptying the recirculating bubble. In this regime the static mode orientation is imposed by the blowing symmetry. Lateral L and R (resp. top/bottom T and B) blowing configurations select P or N states in the horizontal (resp. vertical) direction, while bistable dynamics persists for the symmetric LR and TB configurations. The shape of periodic modes follows the changes in wake static orientation, and Strouhal numbers are barely modified. The transition between the two regimes is governed by both the total injected flow rate and the location of the injection.

Key words: Sensitivity, local blowing, instability control, 3D wakes

† Email address for correspondence: jignacio@ujaen.es

1 **1. Introduction**

2 The seminal work of Wood (1964) considers a blunt trailing edge airfoil with base
3 height h implemented with a central bleed slit of width d . Wood (1964) shows that the
4 base drag decreases almost independently to the blowing jet momentum, determined by
5 the mean jet velocity U_b (also related to the slit's width d) when the volumetric bleed
6 coefficient $C_q = dU_b/hU_\infty$ is increased from zero. However, the maximum drag reduction
7 depends on the blowing jet momentum, which is reached for a flow rate coefficient that is
8 larger as the jet velocity becomes smaller. Increasing further the flow rate coefficient leads
9 to an asymptotic regime of base drag increase with a constant slope. Below the optimal
10 value for base drag reduction, the vortex formation length measured as the distance from
11 the base to the point of maximum velocity fluctuations in the wake moves downstream.
12 This correlation is clarified by Bearman (1967) showing the unique affine relationship
13 of base drag with the inverse of the formation length. Formation lengths varying from
14 $0.3h$ to $1.1h$ were obtained with different wake controls applied to a D-shaped cylinder
15 involving base blowing/suction or splitter plates. Both works report a variation of the
16 Strouhal number of the periodic mode with mass bleed that first augments by 20% and
17 then decreases with a similar magnitude before the disappearance of a definite wake
18 frequency. To the authors knowledge, there is no equivalent incompressible experimental
19 investigations of mass injection for three-dimensional bodies in the literature. Actually
20 most of the research has focused on compressible flows with transonic and supersonic
21 regimes of axisymmetric bodies (Tanner 1975; Viswanath 1996).

22 The incompressible wake dynamics of three dimensional bluff bodies involve few
23 dominant modes. The static mode shape of the rectangular (Grandemange *et al.* 2012)
24 or circular (Rigas *et al.* 2014) base has a permanent asymmetry or deflection in a lateral
25 direction defined by an azimuthal phase. The mode is reminiscent of the first steady
26 symmetry breaking bifurcation at low Reynolds number (Fabre *et al.* 2008; Grandemange
27 *et al.* 2012; Jiménez-González *et al.* 2013, 2014). In the turbulent regime, the static
28 mode undergoes long-time stochastic dynamics that restore statistically the experimental
29 symmetry. The typical time scale is about 100 to 1000 orders of magnitude larger
30 than the convective time scale thus justifying the name of static mode. For circular
31 base, Rigas *et al.* (2015) showed that the azimuthal phase of the static mode follows a
32 diffusive dynamics. For the rectangular base studied by Grandemange *et al.* (2013a,b)
33 with different aspect ratio, the stochastic phase dynamics is restricted to random switches
34 and drifts between two opposite azimuthal phases aligned with the major axis of the base.
35 The case of a perfect reflectional symmetry of the full geometry (involving supports
36 and wall proximity) in the major axis direction of the rectangular base leads to a
37 bistable dynamics between two equiprobable mirrored states (Varon *et al.* 2017). The
38 antisymmetric oscillating mode is characterized by a single frequency with a Strouhal
39 number of approximately 0.2 for circular base (see Sakamoto & Haniu (1990) for a
40 sphere). In case of elliptical or rectangular bases (Kiya & Abe 1999), there are two
41 different Strouhal numbers with the higher (resp. smaller) frequency corresponding to
42 lateral antisymmetric oscillations aligned with the minor (resp. major) axis of the base.

43 Base blowing has been used for bodies with rectangular base essentially to control the
44 free shear layers for drag reduction (Rouméas *et al.* 2009; Wassen *et al.* 2010; Littlewood
45 & Passmore 2012). For these cases, large momentum equal to or larger than that of the
46 incoming flow is injected through perimetric slits located at proximity of separations.
47 Drag reduction is found to be sensitive to the jet orientation, and optimal when jets are
48 orientated inwards the centre of the base. It is related to the change of the free shear layers
49 angle at separation that recalls the beneficial boat tailing effect on drag of square-back

bodies (Wong & Mair 1983). For unclear reasons likely to be produced by the turbulent modelling, both uncontrolled computed flows of Rouméas *et al.* (2009) and Wassen *et al.* (2010) do not reproduce the expected horizontal asymmetry due to the static mode (Grandemange *et al.* 2013a). These have been since retrieved numerically by Pasquetti & Peres (2015); Lucas *et al.* (2017) and Dalla Longa *et al.* (2019). Interestingly, Wassen *et al.* (2010) triggered the static mode for few blowing cases even so respecting the reflectional symmetry. Attempts to control the static mode was recently made using pulsed jets, known to have much more authority on free shear layers than continuous blowing at lower mass injection rate (Greenblatt & Wagnanski 2000). Barros *et al.* (2016b) and Li *et al.* (2016) showed that pulsed jets on one side of the base actively selects the orientation of the static mode. Such flow control strategy has been widely used in fast-back geometries to achieve wall reattachment, providing important drag reduction. However, the wake topology is very different from that of the square-back body, and therefore is out of the scope of the present work.

In addition to jets actuation, there have been several investigations to control the static mode either passively with steady disturbances placed around the body (Grandemange *et al.* 2014; Cadot *et al.* 2015; Barros *et al.* 2017), with a base cavity (Evrard *et al.* 2016; Lucas *et al.* 2017; Bonnavion & Cadot 2018), with base boat-tailing (Perry *et al.* 2015; Pavia *et al.* 2016; Bonnavion & Cadot 2019) or actively with flaps (Brackston *et al.* 2016; García de la Cruz *et al.* 2017; Brackston *et al.* 2018). Overall, three main effects have been observed. First, the selection of the asymmetry orientation related to the symmetry breaking introduced by the device is reported by most of the works. In that case bistable dynamics is suppressed but the static mode still persists with a same or different asymmetry strength. Second, the static mode asymmetry is reduced, still associated with wide global wake fluctuations but having as most probable event a symmetric wake (Grandemange *et al.* 2014; Cadot *et al.* 2015; Li *et al.* 2016; Brackston *et al.* 2016). Third, a full stabilization of the static wake mode towards a symmetric wake. To the authors knowledge, only the base cavity (Evrard *et al.* 2016) was able to fully suppressed the static mode. Concerning the periodic modes, Barros *et al.* (2016a) investigated the resonance behavior of the modes excited with pulsed jets.

Axisymmetric bodies with homogenous base bleed have been investigated theoretically in Sevilla & Martínez-Bazán (2004); Sanmiguel-Rojas *et al.* (2009) and Bohorquez *et al.* (2011) through linear stability analysis. They show a stabilization of both the first steady and second periodic instabilities. The stabilization of the second instability is supported by flow visualization of vortex shedding suppression but no experimental evidence of the inhibition of the static mode strength (reminiscent of the first instability) is reported.

The aim of the work is to investigate the effect of base blowing in a three-dimensional wake with a specific focus on the recently identified static mode (Grandemange *et al.* 2013a) and the antisymmetric periodic modes. The following fundamental questions have not been yet addressed : does base blowing mitigate the strength of the static mode? for which blowing intensity and location blowing has control authority on the orientation of the static mode? Our experimental study is based on the same geometry as Grandemange *et al.* (2013a) with additional blowing slits at different locations of the base. The paper is organized as follows. The experimental set-up is described in §2. Results in §3 first present a reminder of the wake modes identification in §3.1 followed by the effect of base blowing on the base drag in §3.2. The sensitivity analyses of the static and periodic modes are respectively investigated in §§3.3 and 3.4. The mean flow modifications are studied for the wake momentum in §3.5 and recirculating length in §3.6. The results lead to 3 discussions in §4, about the modes sensitivity in §4.1, the drag reduction mechanism

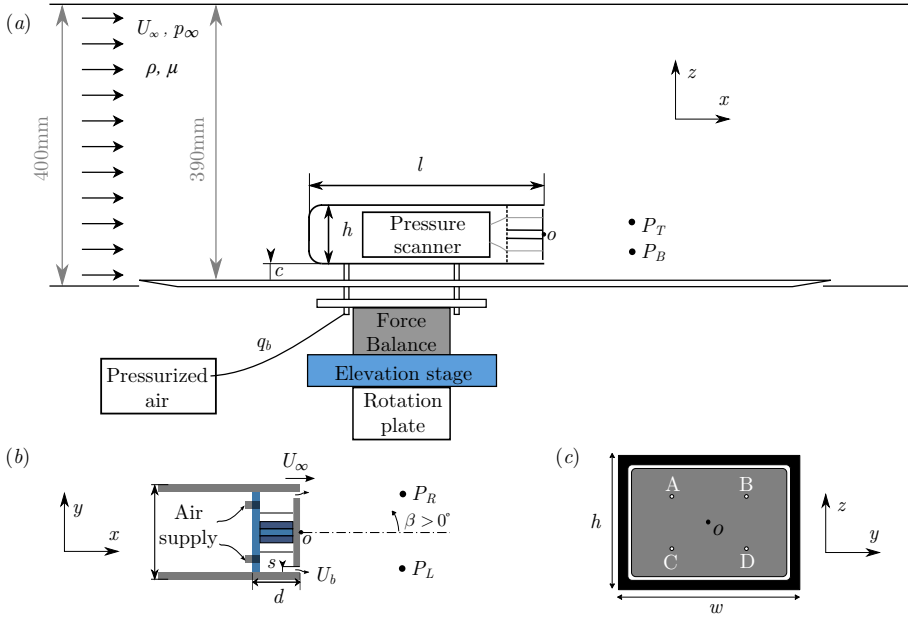


Figure 1: (a) Sketch of the experimental set-up. (b) Top view of the body, showing the internal arrangement of the blowing system. (c) Rear view of the bluff body depicting the 4 pressure tap positions labelled A, B, C, D and the rectangular slit as the white rectangle. The labels P_T , P_B , P_L and P_R in (a,b) indicate the locations for hot wire measurements.

99 in §4.2 and the critical blowing to achieve optimal base drag reduction in §4.3. The
 100 conclusion in §5 ends the paper.

101 2. Experimental set-up

102 2.1. Model geometry, blowing device and wind tunnel

103 A three dimensional body of length $l = 291$ mm, width $w = 97.25$ mm and height h
 104 $= 72$ mm, whose geometry corresponds to the square-back model used by Ahmed *et al.*
 105 (1984), is placed over a ground plate as shown in Fig. 1. It is held by four cylindrical
 106 supports of 7.5 mm diameter (i.e. $0.104h$) leaving a ground clearance of $c/h = 0.278$. The
 107 model is mounted on a turntable to adjust the yaw angle β of the body (rotation with
 108 respect to the z -axis) with an accuracy of 0.01° .

109 The rear of the body is constituted of a frame of depth $d/h = 0.417$ (see Fig. 1b)
 110 creating an internal cavity partially blocked at the base by a central plate. The plate
 111 is smaller than the cavity dimensions to leave a rectangular perimetric slit of width
 112 $s/h = 0.028$ as depicted by the white rectangle in Fig. 1(c). The cavity is pressurized by
 113 injecting air through 4 internal tubes (sketched in Figs. 1b,c) with a steady controlled
 114 flow rate q_b . The velocity produced at the slit denoted U_b is illustrated in Figs. 1(a,b). The
 115 blowing system is connected to a 6 bar compressed air-feeding line through a pneumatic
 116 tube with an Aalborg digital mass flow meter, an air valve and a pressure regulator,
 117 which ensures stability and constancy of the flow rate q_b .

118 Seven blowing configurations shown in Fig. 2 are realized by partially blocking the
 119 rectangular slit by leaving open either one side (asymmetric configurations) or both

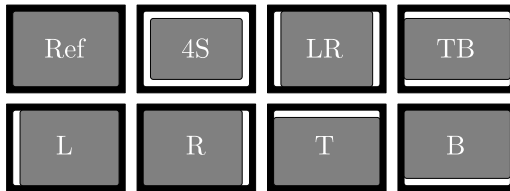


Figure 2: Sketch views of the rectangular base showing the reference case and the open slits configurations used for base blowing (see text). The open slits appear white on the rectangular base.

120 opposite sides (symmetric configurations). The slits were blocked using aluminium tape
 121 placed on marked positions to assure repeatability. These configurations allow to explore
 122 the sensitivity to different spatial distribution of blowing. The good symmetry properties
 123 of the injection is attested in Fig. 3 showing the velocity U_b along the active slits and in
 124 the absence of wind. The configurations are shown in Fig. 3; left (L), right (R), top (T),
 125 bottom (B) for asymmetric configurations, and both left and right (LR), both top and
 126 bottom (TB). As shown in Fig. 3, the lateral blowing configurations produce a nearly
 127 homogeneous profile. However, in the case of the top/bottom configurations, the blowing
 128 velocity is lower at the central part of the slit, although the velocity profiles are clearly
 129 symmetric in the longitudinal direction. Thus, the blowing inhomogeneity along a slit
 130 respects satisfactorily the reflectional symmetries of the rectangular base. Consequently,
 131 the blowing of the symmetric configurations is symmetric, and each blowing of the 4
 132 asymmetric configurations only breaks the reflectional symmetry of the base as it has
 133 been designed for. The symmetric configuration corresponding to the full rectangular slit
 134 did not have the expected symmetry and this configuration cannot be used as a spatially
 135 controlled disturbance of the wake mode. Nevertheless, passive effect will be shown.

136 The uniform wind is produced in an Eiffel-type wind tunnel with a 3/4 open jet
 137 facility of 390 mm \times 400 mm aperture (identical facility of Grandemange *et al.* (2013a)).
 138 The wind speed is fixed at $U_\infty = 20$ m/s with a turbulent intensity below 0.5% and a
 139 spatial inhomogeneity smaller than 0.3%. The Reynolds number based on the height h
 140 of the body is $Re = U_\infty h / \nu \approx 10^5$, where ν is the kinematic viscosity of air. The flow
 141 rate blowing coefficient is defined as $C_q = q_b / (U_\infty w h)$ and the velocity ratio blowing
 142 coefficient as $C_u = q_b / (U_\infty S_b)$ where S_b is the total blowing surface composed of the sum
 143 of the active slits surfaces. The maximum blowing coefficient investigated in the paper
 144 is $C_q = 0.0185$ which corresponds to $C_u = 1.1$ in the single lateral slit configuration.

145 The origin of the cartesian coordinate system (x, y, z) is placed at the center of the
 146 body base, being x the streamwise direction, z the transverse direction normal to the
 147 ground, and y the side direction that forms a direct trihedral. The velocity vector can
 148 be therefore decomposed into respective components $\mathbf{u} = (u_x, u_y, u_z)$. The origin of the
 149 yaw angle is defined as in Evrard *et al.* (2016), $\beta = 0$ corresponds to a bistable dynamics
 150 with equal probability of both deflected wake states. The difference with the geometrical
 151 alignment is 0.22° .

152 For the remainder of the paper, h , U_∞ , and h/U_∞ will be used as characteristic length,
 153 velocity and time scales respectively. We denote with an asterisk *, the dimensionless
 154 variables defined from these characteristic scales. Notation St , for Strouhal number is
 155 used to designate a non-dimensional frequency using h and U_∞ .

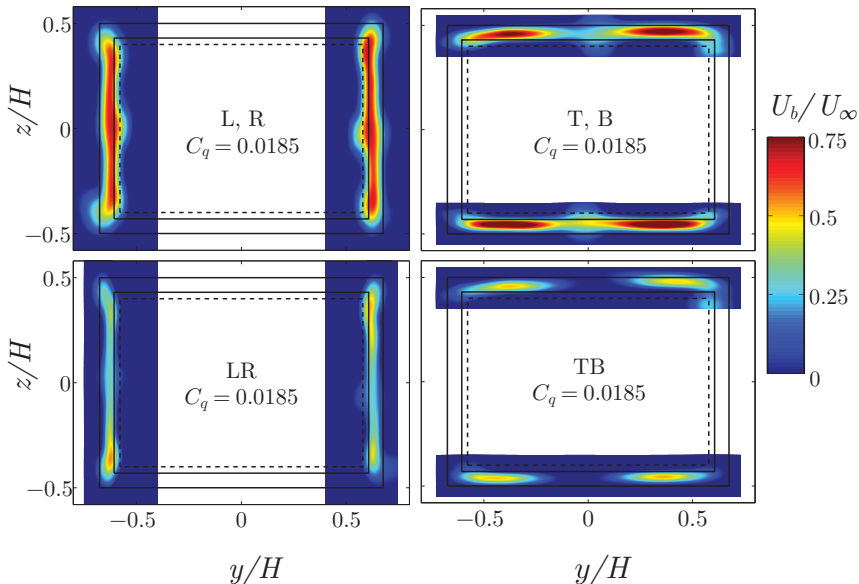


Figure 3: Contours of time-averaged blowing velocity obtained by means of hot wire anemometry measurements at $x/H = 0.1$ and no wind for the 6 blowing configurations: (a) left (L) or right (R); (b) top (T) or bottom (B); (c) both left and right (LR), (d) both top and bottom (TB). The non-dimensional blowing velocity is computed as U_b/U_∞ where $U_\infty = 20$ m/s will be the wind speed used for the remainder of the paper. For all configurations, the corresponding blowing coefficient is $C_q = 0.0185$ (taking $U_\infty = 20$ m/s) that is the maximum value for the experiments.

2.2. Pressure, velocity and force measurements

156

157 Pressure values are measured at four different locations $(y^*, z^*) = (\pm 0.3, \pm 0.2)$ (indi-
 158 cated as A, B, C and D in Fig. 1c). A Scanivalve ZOC22 pressure scanner is placed inside
 159 the model, thus reducing the length of vinyl tubes required to connect the 4 pressure taps
 160 to the pressure sensor. The local pressures at the base are recorded at a sampling rate of
 161 100 Hz each with an accuracy of ± 3.75 Pa and during 250 s for typical experiments. In
 162 the following, pressure will be expressed as instantaneous pressure coefficient

$$c_p(y^*, z^*, t^*) = \frac{p(y^*, z^*, t^*) - p_\infty}{\rho U_\infty^2 / 2}, \quad (2.1)$$

163 where ρ is the air density, p_∞ is the reference static pressure at the inlet of the test
 164 section.

165 These four measurements are used to assess instantaneously the base drag and the wake
 166 asymmetry as introduced by Grandemange *et al.* (2013b). In particular, such arrangement
 167 can be considered a relevant minimal set of measurements to estimate accurately base
 168 drag and base pressure gradient. The reason is that the wall pressure distribution in
 169 the separated area is at first order almost constant in one direction and affine in the
 170 other perpendicular direction (direction of the asymmetry) as illustrated for different
 171 asymmetry directions by Barros *et al.* (2017). The drag is evaluated through the base
 172 drag or suction coefficient (Apelt & West 1975; Roshko 1993) calculated as

$$c_B(t^*) = -\frac{1}{4} \sum_{i=1}^4 c_p(y_i^*, z_i^*, t^*), \quad (2.2)$$

173 The precision on mean pressure coefficients, and then mean base drag is estimated
 174 to ± 0.001 . The wake asymmetry, as previously satisfactorily investigated in Grande-
 175 mänge *et al.* (2013a) and Bonnavion & Cadot (2018), is assessed by means of the non-
 176 dimensional base pressure gradient whose horizontal and vertical components, g_y and g_z ,
 177 are computed as

$$g_y = \frac{\partial c_p}{\partial y^*} \simeq \frac{1}{2} \left[\frac{c_p(y_B^*, z_B^*, t^*) - c_p(y_A^*, z_A^*, t^*)}{y_B^* - y_A^*} + \frac{c_p(y_D^*, z_D^*, t^*) - c_p(y_C^*, z_C^*, t^*)}{y_D^* - y_C^*} \right]; \quad (2.3)$$

$$g_z = \frac{\partial c_p}{\partial z^*} \simeq \frac{1}{2} \left[\frac{c_p(y_A^*, z_A^*, t^*) - c_p(y_C^*, z_C^*, t^*)}{z_A^* - z_C^*} + \frac{c_p(y_B^*, z_B^*, t^*) - c_p(y_D^*, z_D^*, t^*)}{z_B^* - z_D^*} \right]. \quad (2.4)$$

178 Polar coordinates are also useful representation of the gradient since the modulus $g =$
 179 $\sqrt{g_y^2 + g_z^2}$ is related to the strength of the wake asymmetry and the phase angle $\varphi =$
 180 $\arccos(g_y/g)$ to its orientation. The mean pressure gradient precision deduced from that of
 181 the mean pressure coefficient given above is ± 0.003 and ± 0.005 for the y and z component
 182 respectively.

183 In order to make accurate and repeatable base pressure measurements, we leave the
 184 wind tunnel working and the pressure scanner acquiring during about two hours before
 185 investigating one blowing configuration. Experiments are started when no drifts from
 186 the sensor signal are observed. We first acquire the non-blowing case, and then, we
 187 increase by increments the blowing flow rate until the maximum value $C_q = 0.0185$,
 188 recording pressure signals for each selected blowing rate during 250 s. Once the series are
 189 achieved, a non-blowing case is again measured to remove any residual drift effects during
 190 the experiment. Direct measurements of the relative variation of the mean base drag,
 191 $\Delta C_B(C_q)$, are therefore obtained by subtracting the mean base drag values of blowing,
 192 $C_B(C_q)$, and corresponding non-blowing case of the selected configuration, $C_B(C_q = 0)$.
 193 The protocol is repeated for all configurations. Base drag measurements with no blowing
 194 $C_{B0} = C_B(C_q = 0, U_\infty)$ are realized separately where the mean value obtained with no
 195 wind is subtracted to the mean value with the wind.

196 Near wake velocity fields in the two perpendicular planes $y^* = 0$ and $z^* = 0$ are
 197 investigated to obtain respectively the fields $\mathbf{u}_{xz}^* = (u_x^*, 0, u_z^*)$ and $\mathbf{u}_{xy}^* = (u_x^*, u_y^*, 0)$
 198 by means of Particle Image Velocimetry (PIV) measurements. The PIV system uses a
 199 dual pulse laser (Nd:YAG, 2 x 135mJ, 4ns) synchronized with a FlowSense EO, 4 Mpx,
 200 CCD camera. A camera resolution of 2360×1776 pixels, in combination with a 35 mm
 201 focal lens, allows to cover a flow field extension of approximately $x^* = [-0.5, 3] \times y^* =$
 202 $[-1.3, 1.3]$ and $x^* = [-0.3, 2.5] \times z^* = [-0.9, 1.1]$ for measurements in the $z^* = 0$ and
 203 $y^* = 0$ planes respectively, with corresponding pixel resolutions of 0.10 mm/pixel and
 204 0.08 mm/pixel. For typical measurements, 500 pairs of images (using a time delay of
 205 50 μ s between consecutive snapshots) at 10 Hz are acquired. The image masking, PIV
 206 image processing and post-processing of the velocity field obtained, are performed using
 207 a standard PIV cross-correlation algorithm. Velocities are computed in two steps, using
 208 first interrogation window of 32×32 pixels, and then windows of 16×16 pixels, in
 209 both cases with an overlap of 50%. By using this window size, a mesh of 295×222
 210 points for both PIV plane locations was obtained, resulting in a spatial resolution of
 211 $\Delta x = \Delta y = 0.8$ mm (0.011*h*) and $\Delta x = \Delta z = 0.64$ mm (0.009*h*) for planes $z = 0$ and
 212 $y = 0$, respectively.

213 The PIV system is supplemented with a single hot wire probe placed further down-

stream to provide the frequency of the global periodic wake modes. Four measurement locations are investigated, they are shown in Fig. 1 denoted by $P_L = (x^* = 2.5, y^* = -0.5, z^* = 0)$, $P_T = (2.5, 0, 0.3)$, $P_R = (2.5, 0.5, 0)$ and $P_B = (2.5, 0, -0.3)$. The wire is orientated in such a way to measure the modulus u_{xz} for the vertical positions at P_T and P_B and the modulus u_{yz} for the lateral positions at P_L and P_R . The hot wire measurements are sampled at 1 kHz and dominant frequencies are extracted from the power spectral density (PSD), computed using sliding windows of 2 seconds over a signal duration of 120 s, what resulted into a frequency resolution of 0.5 Hz.

The aerodynamic force exerted on the body is measured with a multi-axial load cell (model AMTI-MC3A-100lb) connected to the four cylindrical supports (see Fig. 1). Time series of drag, side and lift components, i.e. f_x , f_y and f_z respectively, are recorded during 60 s at a sampling rate of 1 kHz. The uncertainty of the measurements is estimated (using specifications of crosstalk, non-linearity and hysteresis) to be 0.002 N for the x and y directions and 0.006 N for the z direction, due to its bigger range. The drag, side and lift coefficients are defined as

$$c_i = \frac{f_i}{h\nu\rho U_\infty^2/2}, \quad (2.5)$$

with a corresponding uncertainty of approximately ± 0.001 for c_x , c_y and ± 0.003 for c_z .

Since we are interested in values without the thrust and slits head loss produced by the blowing itself, we subtract to the mean force $F_i = F_i(C_q, U_\infty)$ obtained for a given blowing and wind speed, the mean force at the same blowing but with no wind $F_i(C_q, U_\infty = 0)$. Thus, the mean value

$$\tilde{C}_i = \frac{F_i(C_q, U_\infty) - F_i(C_q, U_\infty = 0)}{h\nu\rho U_\infty^2/2} \quad (2.6)$$

is supposed to be the force coefficient when blowing jet effects are removed. For accurate measurements of \tilde{C}_i we operate as follows. For each C_q and in a single acquisition run, we measure with blowing alone for 15 s (wind tunnel switched off), we then turn on the wind tunnel to capture 30 s of aerodynamic force, and stop the wind tunnel to measure again with blowing alone for another 15 s. Making the average of the two blowing alone stages, and subtracting to the mean force measured during 30 s, we obtain \tilde{C}_i . Measurements of C_i with no blowing are realized separately where the mean value obtained with no wind is subtracted to the mean value with the wind.

Conditional statistics are realized on any measurements presented above to extract the characteristics of the P or N state (Grandemange *et al.* 2013b). They correspond to events such that the horizontal component of the pressure gradient $g_y > 0$ (for P state) or $g_y < 0$ (for N state). For the remainder of the paper, we will denote by a superscript P or N the conditional averaging of any variables following this rule. Pressure is always simultaneously recorded with the PIV measurements to proceed for conditional averaging on the velocity fields.

The following notation is used: time dependent variables are denoted by lower case letters a , time-averaged values by upper case letters $A = \bar{a}$ and standard deviations by $A' = \sqrt{(a - A)^2}$. As defined previously, conditional statistics denoted A^i and A'^i are respectively the average and standard deviation of the $i = P$ or N state. We will use the notation $A_0 = A(C_q = 0)$ for measurements with no blowing and ΔA for a difference with the non-blowing case : $\Delta A = A(C_q) - A_0$.

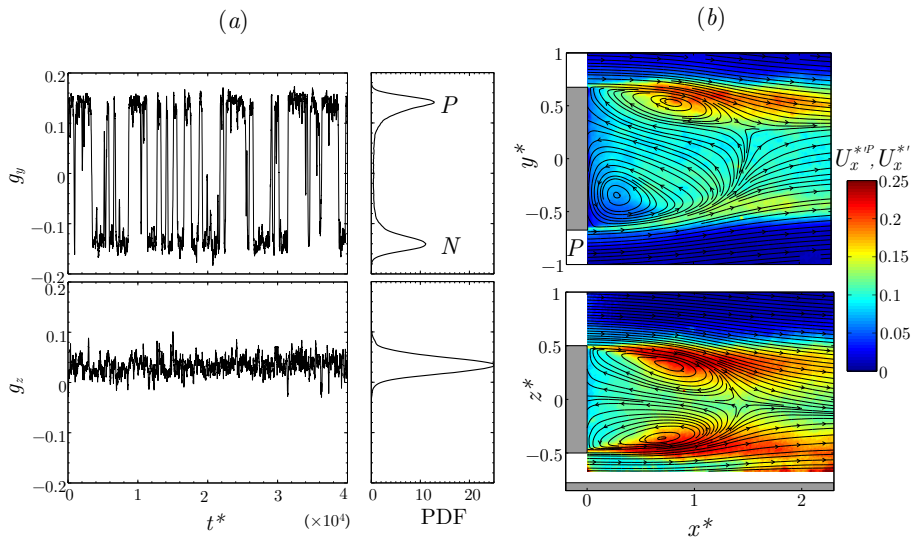


Figure 4: Reference case (no slits) : (a) time series of the pressure gradient components $g_y(t^*)$, $g_z(t^*)$ and their corresponding probability density functions (PDF). (b) Streamlines of the mean velocity field \mathbf{U}_{xy}^{*P} (top), \mathbf{U}_{xz}^* (bottom) superimposed to the velocity fluctuations U_x^{*P} (top), U_x^* (bottom).

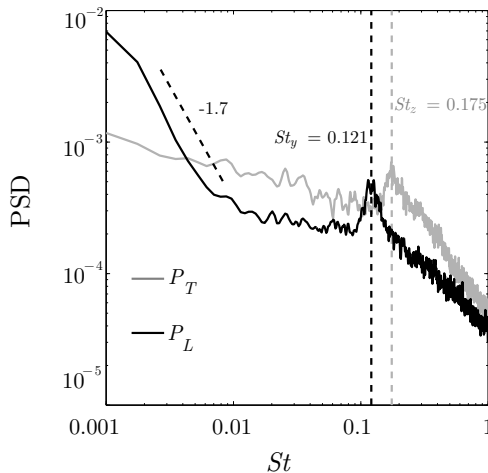


Figure 5: Reference case (no slits): power spectral density of the local velocity at P_T and P_L (see Fig. 1). The resonant peaks indicate the presence of the periodic asymmetric modes of the wake with a high frequency $St_z = 0.175$ for the vertical mode and a low frequency $St_y = 0.121$ for the horizontal mode (Grandemange *et al.* 2013a).

255 3. Results

256 We now present the flow at $Re = 10^5$. The results section is organized as follows.
 257 It starts with a preliminary characterization of the reference case (no slits) and then
 258 takes into account the different configurations of open slits without blowing in §3.1. Two
 259 regimes of blowing referred to as mass and momentum are evidenced in §3.2 on the basis
 260 of base drag measurements. The detailed investigations of the wake is focusing on the

C_x^{Ref}	0.371	C_y^{Ref}	0.002	C_z^{Ref}	-0.055	C_B^{Ref}	0.177
$C_x'^{\text{Ref}}$	0.005	$C_y'^{\text{Ref}}$	0.019	$C_z'^{\text{Ref}}$	0.010	$L_r^{*\text{Ref}}$	1.45
G^{Ref}	0.133	G_z^{Ref}	0.037	$G_y^{P,\text{Ref}}$	0.127	$G_y^{N,\text{Ref}}$	-0.126
St_y	0.121	St_z	0.175				

Table 1: Reference case (no slits): mean values of force coefficients, base drag, recirculating bubble length, base pressure gradient modulus of the static mode with components for its N and P states, Strouhal numbers of the periodic modes.

261 static symmetry breaking modes in §3.3 and then on the periodic modes in §3.4. The
 262 path of the injected mass is assessed for the two blowing regimes in §3.5 and finally,
 263 section §3.6 characterizes the correlation of the recirculating length and the base drag.

264 3.1. Flow without blowing

265 The wake of the body with the additional rear device without open slits at the base is
 266 referred to as the reference case. It exhibits the well known long-time bistable dynamics
 267 due to the y -instability as reported in Grandemange *et al.* (2013a,b). This behavior is
 268 clearly observed by the random switches of the horizontal component of the pressure
 269 gradient g_y in Fig. 4(a). They occur between two well defined mirrored states denoted
 270 P and N in the corresponding probability density function. The time spent in one
 271 state can be as large as few orders of magnitudes of the convective time scale. The
 272 vertical component of the pressure gradient g_z remains almost insensitive to the switching
 273 dynamics in Fig. 4(a). Its positive value is introduced by the presence of the body support
 274 and the ground. The wake topology corresponding to the P state is obtained in Fig. 4(b)
 275 and reveals the static mode of the wake as reported in the literature. The N state (not
 276 shown here) is a mirror symmetry ($y^* \rightarrow -y^*$) of the P state.

277 The two periodic modes of the wake are identified in the PSD shown in Fig. 5 of
 278 the local velocity measurements in the wake. In accordance to the wake characterization
 279 of Grandemange *et al.* (2013a), we find a low resonant frequency denoted $St_y = 0.121$
 280 (captured by the local velocity at P_L) associated with the global lateral motion and a
 281 high resonant frequency denoted $St_z = 0.175$ (captured by the local velocity at P_T)
 282 associated with the global vertical motion. In addition, the random bistable dynamics in
 283 the horizontal direction can be identified in the PSD of P_L with the -1.7 decay for low
 284 values of St .

285 Table 1 summarizes the main global flow characteristics of the reference case such as
 286 force coefficients, recirculating bubble length, base drag and mean pressure gradient.
 287 Recirculation region extension has been characterized as the maximum downstream
 288 location from the body base where $U_x^* \leq 0$. All these values are in accordance with
 289 previous measurements for similar square-back geometries. However, strict comparison
 290 with other published works is meaningless because none of the geometries are identical
 291 with significant variations such as forebody shape, supports design, ground clearance
 292 and body dimensions. In this regard, the present drag coefficient $C_x^{\text{Ref}} = 0.371$ obtained
 293 with a body length $l^* = 4$ and a ground clearance $c^* = 0.278$ is substantially larger
 294 than $C_x = 0.274$ obtained by Grandemange *et al.* (2013a) with a body length $l^* = 3.6$
 295 and a ground clearance $c^* = 0.174$. It is worth to mention that for both cases the base
 296 drag is similar, $C_B = 0.177$ in the present case and $C_B = 0.185$ in Grandemange *et al.*
 297 (2013a). The drag discrepancy can be reasonably explained by the additional length of
 298 the cylindrical supports together with the friction introduced by the body extension.

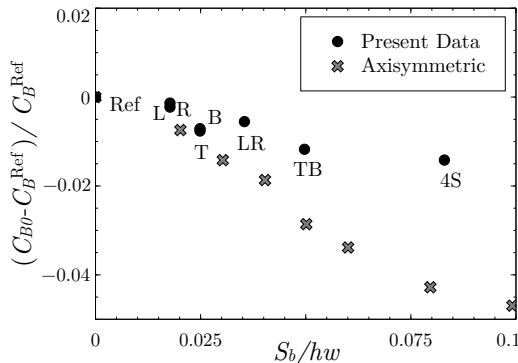


Figure 6: Base drag modification for all slit configurations as displayed in Fig. 2 without blowing versus slits area. The axisymmetric data are from García de la Cruz *et al.* (2017).

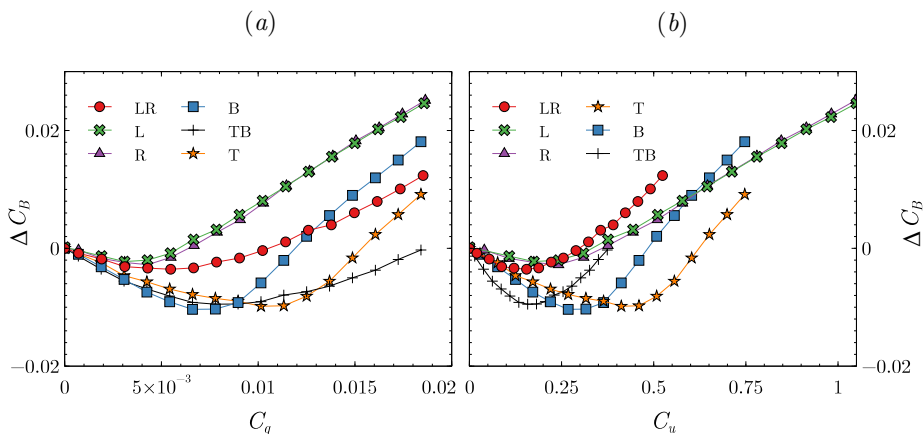
299 We can see in table 1 that the floor and supports produce a negative lift coefficient
 300 $C_z = -0.055$, the bistable dynamics between the two asymmetric states is responsible
 301 for the large fluctuation in the side force coefficient $C'_y = 0.019$ due to the random
 302 switches of the y component of pressure gradient between the mean values of both states
 303 $G_y^{N,Ref}$ and $G_y^{P,Ref}$. The mean pressure gradient modulus $G^{Ref} = 0.133$ gives the strength
 304 of the permanent wake asymmetry.

305 We denote by C_{B0} the base drag obtained for each slits configuration as displayed in
 306 Fig. 2 without injection, i.e. $C_q = 0$. Whatever the configuration, a slight reduction of
 307 C_{B0} is obtained from the reference case. This effect due to open slits at the base was
 308 also found by Bearman (1967) for a two-dimensional blunt body and García de la Cruz
 309 *et al.* (2017) for an axisymmetric blunt body. The relative change of base drag coefficient
 310 $(C_{B0} - C_B^{Ref})/C_B^{Ref}$ is shown in Fig. 6 against the slits area normalized by the base area,
 311 S_b/hw . The decrease obtained by García de la Cruz *et al.* (2017) with a perimetric slit on
 312 a circular base is also reported in the figure. The rectangular perimetric slit (configuration
 313 4S) is shown for comparison with the circular perimetric slit. A much smaller relative base
 314 drag decrease is observed with the wake of the rectangular base that is approximately
 315 1.5% compared to the 4% of the circular base. This reduction is interpreted in García
 316 de la Cruz *et al.* (2017) as an effect associated with a decrease of the intensity of the
 317 wake asymmetry and likely to be produced by the stabilization of the static mode. In
 318 order to check this result in our geometry, table 2 shows base drag and mean pressure
 319 gradients for all configurations. In contradiction, it appears that as a general trend in our
 320 accuracy, the asymmetry strength given by G_0 is rather increased in comparison to the
 321 reference value of 0.133 with open slits. However, according to the precision of ± 0.005
 322 for the mean pressure gradient and ± 0.001 for the base drag, these weak effects seem
 323 unfortunately at the limit of our measurements that may lead to unreliable conclusions.
 324 A significant effect is however detectable on the z component of the pressure gradient
 325 for B and T configurations pointing out a local pressure increase on the side of the open
 326 slit thus enhancing the vertical component in the T configuration and reducing it in the
 327 B configuration.

3.2. Blowing effect on the base drag

329 The base drag variation $\Delta C_B = C_B - C_{B0}$ is shown for all configurations as a function
 330 of C_q in Fig. 7(a) and C_u in Fig. 7(b). We recall that the L and R configurations are
 331 symmetrically equivalent explaining why the corresponding curves are superimposed.

Configuration	L	R	T	B	LR	TB	4S
C_{B0}	0.176	0.176	0.175	0.175	0.176	0.175	0.174
G_{y0}^P	0.129	0.129	0.127	0.128	0.134	0.133	0.135
G_{z0}^P	0.035	0.036	0.047	0.031	0.037	0.038	0.036
G_{y0}^N	-0.127	-0.127	-0.125	-0.125	-0.131	-0.130	-0.133
G_{z0}^N	0.037	0.038	0.049	0.033	0.039	0.040	0.038
G_0	0.135	0.135	0.136	0.131	0.139	0.138	0.140

 Table 2: Passive effect values ($C_q = 0$) for all configurations.

 Figure 7: Base drag coefficient variation $\Delta C_B = C_B - C_{B0}$ versus the flow rate coefficient C_q (a) and blowing velocity ratio C_u (b).

Configuration	L	R	T	B	LR	TB
$C_q^{\text{Opt}} (10^{-3})$	4.3	4.3	10.2	6.6	5.5	7.8
C_u^{Opt}	0.242	0.242	0.412	0.268	0.155	0.158
BDR (%)	1.5	1.6	5.7	6.2	2.1	5.5
$\frac{\partial C_B}{\partial C_q} _0$	-0.78	-0.79	-1.07	-1.65	-0.99	-1.51
$\frac{\partial C_B}{\partial C_u} _\infty$	0.036	0.036	0.074	0.072	0.049	0.052
b_∞	-0.014	-0.014	-0.046	-0.035	-0.014	-0.020

 Table 3: Data extracted from Fig. 7. Optimal values of base bleed coefficients for maximum base drag reduction $BDR = -\Delta C_B^{\text{min}}/C_{B0}$ for all configurations. Parameters of the linear fit in the mass regime $\Delta C_B = \frac{\partial C_B}{\partial C_q}|_0 C_q$ and in the momentum regime $\Delta C_B = \frac{\partial C_B}{\partial C_u}|_\infty C_u + b_\infty$.

332 A same trend is observed for all configurations, characterized by an initial base drag
 333 reduction with increasing values of the blowing intensity, followed by a constant slope
 334 increase of base drag. This general behavior is similar to that obtained by Wood (1964)
 335 for two-dimensional bodies implementing rear blowing. Two blowing regimes have to
 336 be distinguished, we will refer to as the *mass* regime, the small blowing for which the
 337 base drag is decreased and the *momentum* regime, the larger blowing for which the base

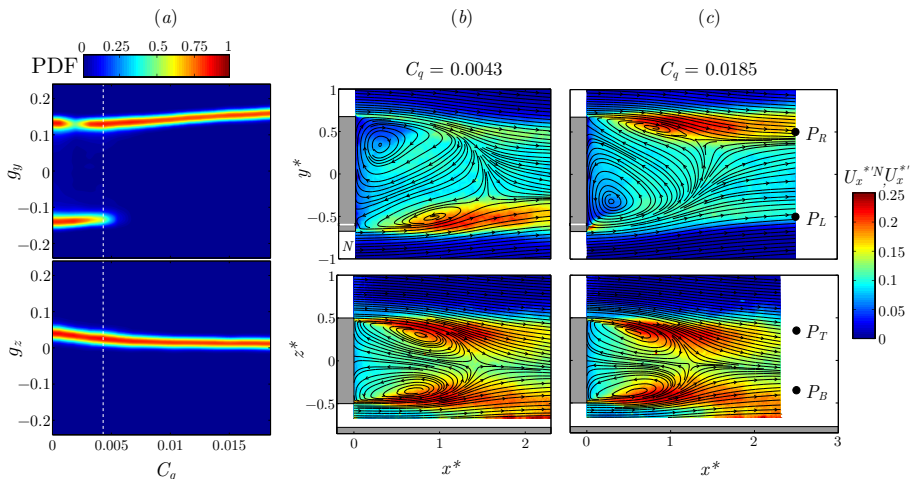


Figure 8: Blowing in L configuration. (a) Sensitivity maps of the Cartesian components, g_y and g_z of the base pressure gradient. The white dashed line marks the C_q^{Opt} value for which the mean base drag C_B is minimum. (b, c) Streamlines of the mean velocity field \mathbf{U}_{xy}^{*N} (top, left), \mathbf{U}_{xz}^{*} (bottom) superimposed to their corresponding velocity fluctuations $U_x'^N$ or U_x' for (b) $C_q^{\text{Opt}} = 0.0043$ and (c) $C_q = 0.0185$. The white band in (b, c) indicates the blowing slit.

338 drag is increased. Both regime are fitted with linear regressions whose parameters are
 339 given in table 3. The maximum of base drag reduction, BDR (approximately from 1% to
 340 7%) and the corresponding optimal blowing coefficients, C_q^{Opt} and C_u^{Opt} , summarized
 341 in table 3 show a substantial dependency with the blowing configuration. Maximal
 342 reductions involve the top or bottom slits whether the configuration is symmetric or
 343 not. The B configuration achieves the best reduction. There is no evidence of simple
 344 relation between either the optimal C_q or C_u and the blowing configurations. This high
 345 and non-trivial sensitivity to the blowing location and intensity is investigated in the
 346 next sections by studying the wake modes interaction with the blowing.

3.3. Static mode

3.3.1. Asymmetric blowing configurations

349 Both configurations L and R have been identically investigated and the experimental
 350 data are, as expected, symmetrically equivalent. For brevity of the paper we only present
 351 results for one configuration, and the results for the other can be deduced by the left to
 352 right reflectional symmetry.

353 The sensitivity map of the Cartesian components of the base pressure gradient for the
 354 L configuration is displayed in Fig. 8(a). As introduced in Bonnavion & Cadot (2018), it
 355 represents the probability density function of the gradient component normalized by the
 356 most probable value computed from each value of the varying parameter, here the blowing
 357 flow rate. The vertical dashed line locates the optimal value of blowing that separates
 358 the mass and momentum regime as defined above. The positive (resp. negative) branch
 359 corresponds to the P state (resp. N state). In the mass regime, $C_q < C_q^{\text{Opt}}$, the dynamics
 360 is bistable involving both P and N states. From the initial case at $C_q = 0$ where both
 361 states are equiprobable, we see a significant change in their probability of presence as
 362 blowing is increased, promoting the N state. The preferential state selection in the mass

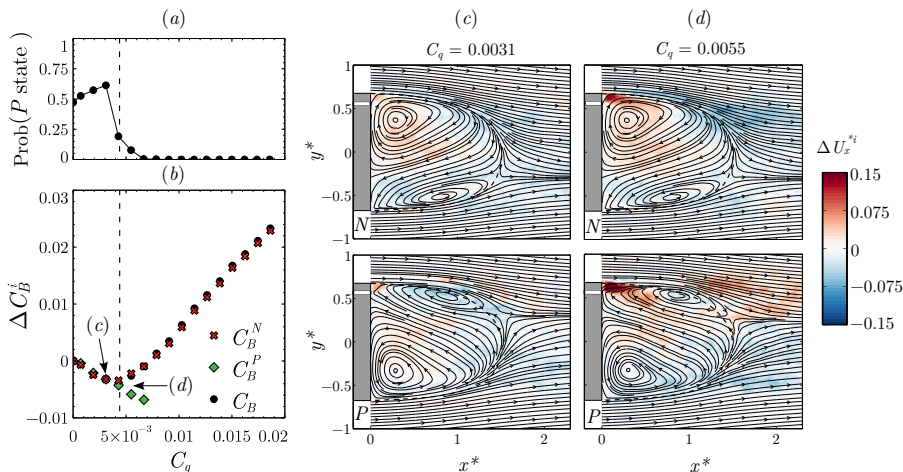


Figure 9: Blowing in R configuration: (a) Probability of occurrence of the P state (top) and relative variation of base drag (bottom) for N and P states versus the blowing coefficient. The dashed line marks the $C_q^{\text{O}pt}$ value for which C_B is minimum. (c, d) Contours of the mean streamwise velocity difference $\Delta U_x^{*i} = U_x^{*i} - U_{x0}^{*i}$ of states $i = P, N$ superimposed to the mean flow streamlines of the field $\mathbf{U}_{\mathbf{xy}}^{*i}$ for $C_q = 0.0031$ (c) and $C_q = 0.0055$ (d). White bands in (c, d) indicate the blowing slits.

363 regime is then opposite to that of the momentum regime. It can be seen that the change
 364 of blowing regime is accompanied with a permanent wake reversal towards the P state
 365 (Fig. 8c) that was predominantly in the N state (Fig. 8b) in the mass regime. The
 366 momentum regime is then associated with a selected P state in L configuration, where
 367 the blowing jet (clearly identified by its large localized fluctuation U_x^* in front of the
 368 slit) is fixing the steady circular recirculation of the bubble. It is also worth mentioning
 369 that there is almost no trace of the blowing jet for the largest blowing in the mass regime
 370 reached when $C_q = C_q^{\text{O}pt}$ in Fig. 8(b). However, a direct effect of the blowing can be
 371 identified through the additional linear increase of g_y in Fig. 8(a). The blowing is likely
 372 to produce a positive pressure gradient proportional to C_q that is not affected by the
 373 wake state whether it is P or N .

374 We now turn to the effect of the L or R blowing during the bistable dynamics. Actually,
 375 there should be a distinction whether the wake is in an N or P state. Depending on the
 376 wake state, the jet blows in either an opposite streamwise velocity region as depicted in
 377 Fig. 8(b,top), or in an adverse streamwise velocity region as depicted in Fig. 8(c,top).
 378 Conditional averaging is thus performed next to distinguish the two cases. Figure 9
 379 presents results obtained with configuration R. During the bistable dynamics that extend
 380 until $C_q = 6.6 \times 10^{-3}$ in Fig. 9(a), the mass regime preferentially selects the P state with
 381 a probability larger than 0.5 while the momentum regime selects the N state. These
 382 are actually the expected results for the R configuration that can be deduced from the
 383 mirror symmetry of the above observations concerning the L configuration described
 384 in Fig. 8. The mean base drag and mean velocity field of each state are respectively
 385 shown in Fig. 9(b) and Figs. 9(c, d). There is no distinctions in the base drag of the two
 386 states until the blowing coefficient reaches $C_q = C_q^{\text{O}pt}$. Bistable dynamics occur as far as
 387 the P state is observable, that extends beyond $C_q^{\text{O}pt}$ until $C_q = 6.6 \times 10^{-3}$. Around this
 388 blowing limit, the velocity fields displayed by the streamlines of the two states in Fig. 9(d)
 389 are globally mirrored from each other, while the corresponding base drag reduction are

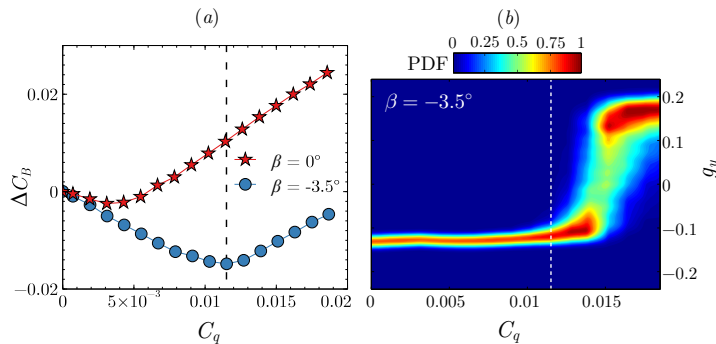


Figure 10: Blowing in L configuration with yaw. Relative variation of base drag (a) versus the injection coefficient for the body yawed at $\beta = -3.5^\circ$. The case $\beta = 0^\circ$ is added for comparison. (b) Sensitivity map of the horizontal component of the base pressure gradient to blowing with the yaw $\beta = -3.5^\circ$. In (b, c), the dashed line marks $C_q^{\text{Opt}} = 0.0115$ for which the mean base drag C_B is minimum.

390 significantly different. The P state is likely to be in a mass regime with a base drag
 391 reduction that is still increasing linearly with the blowing coefficient while the N state
 392 produces a base drag increase characteristic of the momentum regime. We deduce that
 393 it is more favourable for base drag reduction to blow in the opposite velocity flow region
 394 than in the adverse velocity region. Since the blowing jet is hardly discernible in the
 395 mean flows, we superimposed to the streamlines in Fig. 9(c, d) the difference of the mean
 396 streamwise velocity with that of the flow at $C_q = 0$, say $\Delta U_x^{*i} = U_x^{*i} - U_{x0}^{*i}$ where $i = P$ or
 397 N denotes the state. The blowing jet is not discernible in the mass regime in Fig. 9(c) for
 398 both states at $C_q = 0.0031$, indicating that the injected momentum is efficiently mixed
 399 (i.e. dissipated) in the asymmetric recirculating bubble independently to the injection
 400 location. On the other hand, the jet is clearly observable in Fig. 9(d) at $C_q = 0.0055$.
 401 For both states it contributes to increase the momentum, obviously more when located
 402 in the opposite flow region in the P state in Fig. 9(d, bottom) than in the N state in
 403 Fig. 9(d, top).

404 The favourable configuration (injection in the reversed flow region of the bubble) can
 405 be forced by applying a yaw angle β to the body. It has been previously shown (Volpe
 406 *et al.* 2015) that a yaw of 1° is sufficient to permanently selects a P (resp. N) state with
 407 a positive (resp. negative) yaw without any modification of the base pressure gradient
 408 modulus (Bonnaivon & Cadot 2018). Figure 10(a) shows the base pressure variation
 409 where the body has been yawed to $\beta = -3.5^\circ$ to select an N state. As expected, the
 410 mass regime is extended by a blowing in the L configuration compared to the unforced
 411 wake ($\beta = 0^\circ$). It reaches a larger limit value $C_q^{\text{Opt}} = 0.0115$ and an increased maximum
 412 base drag reduction of 7.5%. The sensitivity map of the horizontal component of the
 413 pressure gradient shows that in the mass regime, the gradient magnitude of the forced
 414 N state remains unchanged until bistable dynamics appear due to compensation effect
 415 (Bonnaivon & Cadot 2018) of asymmetries between yaw and local momentum injection
 416 at the base.

417 The L or R blowing configuration studied above breaks the same symmetry as the static
 418 modes (i.e. left/right symmetry), leading in the momentum regime to the permanent
 419 selection of unique state. Now, we investigate B or T blowing configurations that break
 420 the top/bottom symmetry and will show very different interaction with the wake. The
 421 sensitivity map of the base pressure gradient in the T configuration is shown in Fig. 11(a).

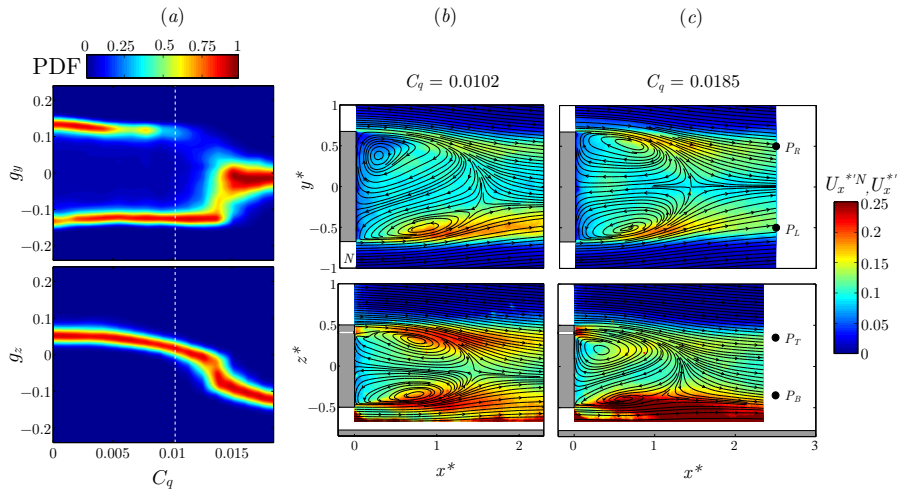


Figure 11: Blowing in T configuration. (a) Sensitivity maps of the Cartesian components, g_y and g_z of the base pressure gradient. The white dashed line marks the C_q^{Opt} value for which the mean base drag C_B is minimum. (b, c) Streamlines of the mean velocity field $\mathbf{U}_{\mathbf{xy}}^{*N}$ (top, left), $\mathbf{U}_{\mathbf{xz}}^*$ (bottom) superimposed to their corresponding velocity fluctuations $U_x'^{*N}$ or $U_x'^{*}$ for (b) $C_q^{\text{Opt}} = 0.0102$ and (c) $C_q = 0.0185$. The white band in (b, c) indicates the blowing slit.

422 A bistable dynamics is observed during the entire mass regime. At the maximum
 423 of drag reduction, the wake topology (Fig. 11b) remains very similar to that of the
 424 reference flow. The momentum regime is first marked by the disappearance of the P
 425 state and then to the suppression of the asymmetry in the y direction since the horizontal
 426 component g_y eventually fluctuates around a unique value equal to zero. This suppression
 427 is simultaneously accompanied with a decrease of the gradient component g_z in the z
 428 direction. It indicates that the blowing at the upper part of the base has rotated the
 429 two states to a single state with a vertical asymmetry leading to a N state in the z
 430 direction. This is clearly illustrated by the velocity fields in Fig. 11(c) for the largest
 431 blowing coefficient. The N state in the z direction that is forced by blowing in the T
 432 configuration actually reproduces the same situation observed in the momentum regime
 433 (Fig. 8c) with the P state in the y direction selected by blowing in the L configuration.
 434 These two cases are deduced from each other by a simple $\pi/2$ rotation.

435 The gradual rotation of the base pressure gradient as the blowing is increased is
 436 better quantified in Fig. 12 that summarizes the base pressure gradient evolution for all
 437 asymmetric blowing configurations. Each point of the plot represents the mean gradient
 438 of a corresponding wake state either P or N obtained through conditional averaging.
 439 By definition, the P branch develops on the right hand side of the plot and the N
 440 branch on the left hand side. The continuous ellipse is modelling all the possible pressure
 441 gradients of the unstable wake (i.e. dominated by a static mode) that would have been
 442 passively selected by steady disturbances of pitch and yaw of the body in absence of
 443 blowing (Bonnavion & Cadot 2018). This view gives useful information about the wake
 444 asymmetry strength measured as the modulus of the gradient. Gradients located on
 445 the initial ellipse indicate no modification of the asymmetry strength compared to that
 446 naturally developed by the body geometry. However, when the blowing is activated, the
 447 wake strength is modified and gradients locate in different magnitude levels, as illustrated

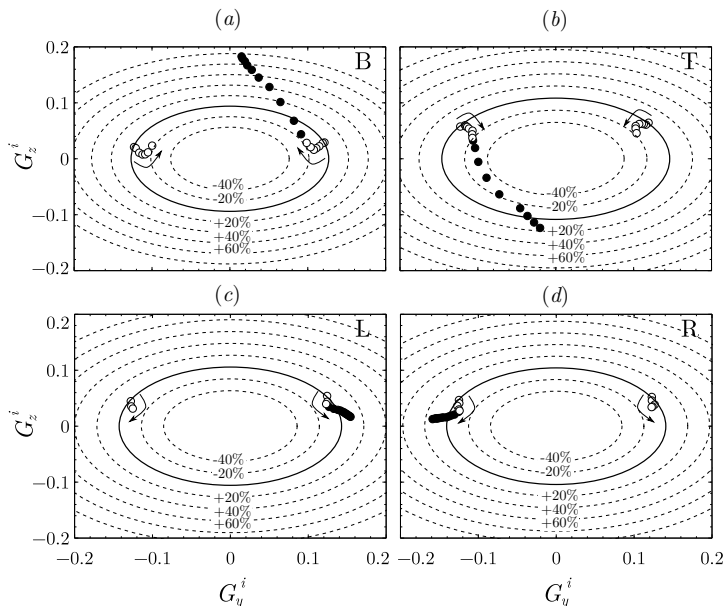


Figure 12: Blowing in asymmetric configurations : (a) T, (b) B, (c) L and (d) R. Mean pressure gradient components of the wake states (G_y^i, G_z^i) with $i = N, P$ in mass regime (empty symbols) and momentum regime (filled symbols). The solid line ellipse is the model of Bonnavion & Cadot (2018) (see text) and dashed ellipses are standing for variations of 20% of the gradient magnitude obtained with no blowing. The arrows indicate gradual increase of the blowing coefficient C_q .

448 in Fig. 12 (see dashed ellipses), where the arrows represent the gradual increase of the
 449 blowing coefficient C_q . In particular, the mass regime (empty symbols) in the T and B
 450 configurations in Fig. 12 (a, b) leads to a decrease of 20% of the initial mean gradient
 451 modulus. However, the momentum regime (filled symbols) in which the rotation occur
 452 shows a significant amplification of the asymmetry likely to be fed by the blowing jet.
 453 The same representation of the gradient of the wake states for the L and R blowing
 454 configuration (Fig. 12 c, d) indicates as well an attenuation of the asymmetry during the
 455 mass regime (approximately 10%) and an amplification in the momentum regime. The
 456 reduction of the asymmetry is mainly ascribed to a decrease of the horizontal component
 457 of the gradient for B or T configurations and of the vertical component for L or R
 458 configurations.

459 3.3.2. Symmetric blowing configurations

460 The two symmetric configurations, either obtained with a simultaneous blowing in
 461 the left and right slits (LR) or top and bottom slits (TB) give very similar results.
 462 The sensitivity maps of the base pressure gradient, respectively given in Fig. 13(a) and
 463 Fig. 14(a) indicate that bistable dynamics are conserved as expected by the blowing
 464 symmetry. The two P and N states remain also very similar whatever the blowing
 465 injection is as can be seen in Fig. 13(b, c) and Fig. 14(b, c). However, the horizontal
 466 gradient component g_y reaches a small value for the optimal blowing coefficient in both
 467 Figs. 13(a) and 14(a) showing that maximum base drag reduction is associated with a
 468 strength reduction of the asymmetry.

469 Fig. 15 recaps the base pressure gradient evolution for the two symmetric blowing.

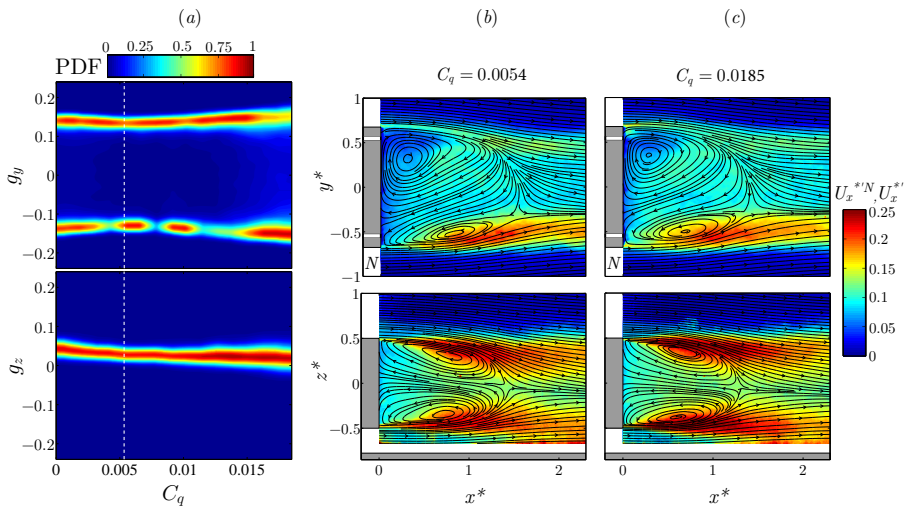


Figure 13: Blowing in LR configuration. (a) Sensitivity maps of the Cartesian components, g_y and g_z of the base pressure gradient. The white dashed line marks the C_q^{Opt} value for which the mean base drag C_B is minimum. (b, c) Streamlines of the mean velocity field \mathbf{U}_{xy}^{*N} (top), \mathbf{U}_{xz}^* (bottom) superimposed to their corresponding velocity fluctuations U_x^{*N} or U_x^* for (b) $C_q^{\text{Opt}} = 0.0054$ and (c) $C_q = 0.0185$. The white bands in (b, c) indicate the blowing slits.

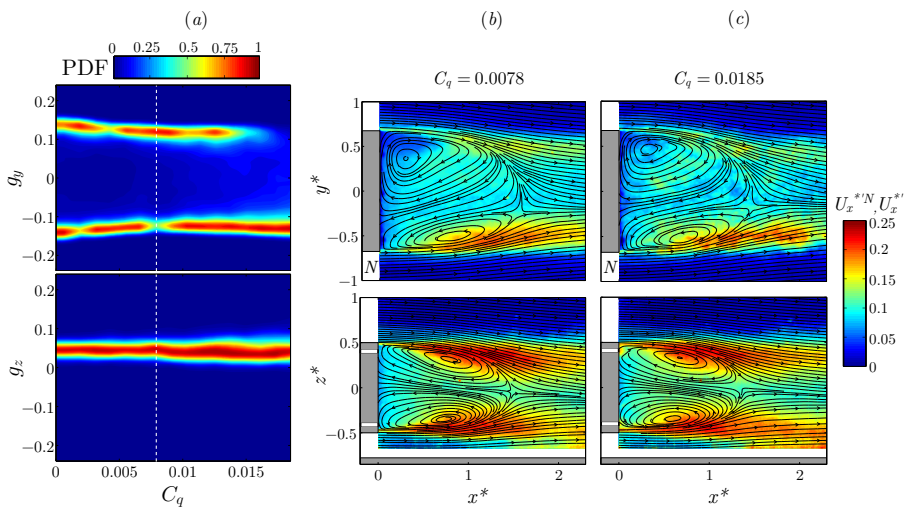


Figure 14: Blowing in TB configuration. (a) Sensitivity maps of the Cartesian components, g_y and g_z of the base pressure gradient. The white dashed line marks the C_q^{Opt} value for which the mean base drag C_B is minimum. (b, c) Streamlines of the mean velocity field \mathbf{U}_{xy}^{*N} (top), \mathbf{U}_{xz}^* (bottom) superimposed to their corresponding velocity fluctuations U_x^{*N} or U_x^* for (b) $C_q^{\text{Opt}} = 0.0078$ and (c) $C_q = 0.0185$. The white bands in (b, c) indicate the blowing slits.

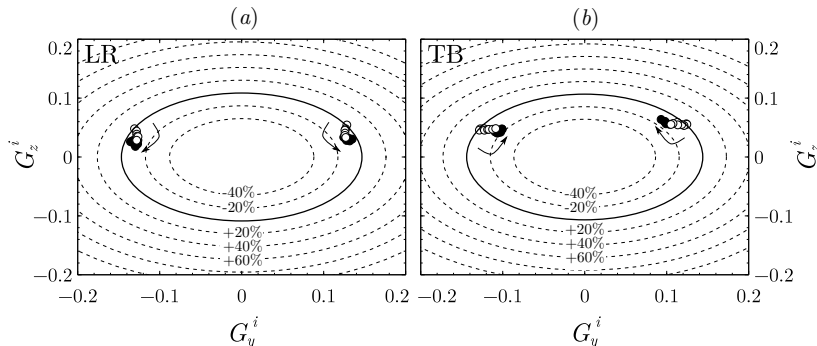


Figure 15: Blowing in symmetric configurations : (a) LR and (b) TB. Mean Pressure gradient components of the wake states (G_y^i, G_z^i) with $i = N, P$ in mass regime (empty symbols) and momentum regime (filled symbols). The solid line ellipse is the model of Bonnavaion & Cadot (2018) (see text commenting Fig. 12) and dashed ellipses are standing for variations of 20 % of the gradient magnitude obtained with no blowing. The arrows indicate the gradual increase of the blowing coefficient C_q .

470 We observe an attenuation of the asymmetry strength given by the mean gradient
 471 modulus of approximately 10% for the LR configuration mainly caused by a decrease
 472 of the vertical component and 20% for the TB configuration due to a decrease of the
 473 horizontal component.

474

3.4. Periodic modes

475 Here, the global periodic modes are studied for steady blowing using the L and T
 476 blowing configurations only, owing each to 3 local points velocity measurements in the
 477 wake. Their locations (see §2.2) are displayed in Fig. 16 with a sketch view towards the
 478 base, but they are also displayed in the velocity fields in Fig. 8 (L blowing configuration)
 479 and Fig. 11 (T blowing configuration) to specify their relative position in the spatial
 480 distribution of the turbulent fluctuations. The power spectral densities are computed
 481 at each location varying the blowing coefficient and displayed as a colormap versus the
 482 non-dimensional frequency St and C_q in Fig. 16(a) for the L configuration and Fig. 16(b)
 483 for the T configuration.

484 The two shedding frequencies initially observed at $St_z \approx 0.121$ and $St_y \approx 0.175$ with
 485 no blowing are clearly identifiable in Fig. 16 when the blowing coefficient is increased. We
 486 can see that the only significant frequency modification is observed for the well defined
 487 low frequency that increases from 0.121 to about 0.15 with wider energy distribution
 488 when blowing in the L configuration in Fig. 16(a). Apart from this effect, the major
 489 changes lie in the intensity of the resonance peaks that directly reflects the anisotropy of
 490 the fluctuations of the static mode together with its interaction with the local blowing
 491 presented in §3.3. Changes in intensities coincide with the transition between the mass
 492 and momentum regime at the optimal blowing C_q^{Opt} . For the L configuration in Fig. 16(a),
 493 the N state is predominantly present in the mass regime such that the probe P_L is
 494 more often in a high level of fluctuation as shown by Fig. 8 (b) than P_R . The situation
 495 inverts in the momentum regime that permanently selects the P state producing high
 496 fluctuation at P_R location and smaller at P_L location as can be seen in Fig. 8 (c). For the
 497 T configuration, the $\pi/2$ rotation of the static mode from horizontal bistability between
 498 P and N states of the mass regime, to a vertical N state at maximum blowing (clearly
 499 observable in Fig. 11) is responsible for the intensity variations in the spectra in Fig. 16

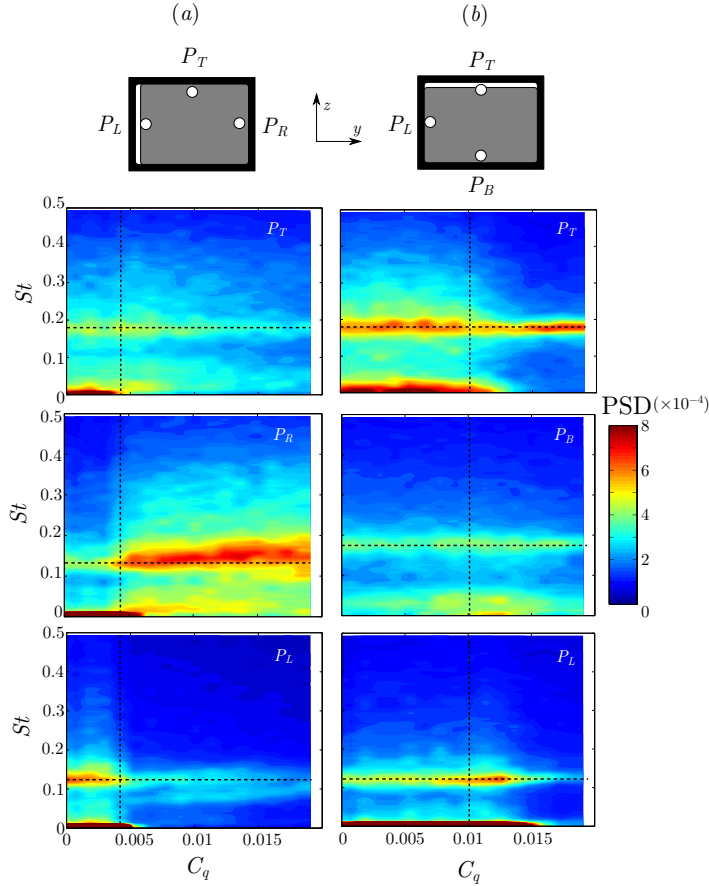


Figure 16: Effect of blowing on the wake periodic modes in L (a) and T (b) configurations. Contours of Power Spectral Density (PSD) of local velocity measured at P_L , P_R , P_T and P_B (see §2.2) as depicted in the top of the figure and also in Fig. 8 and Fig. 11. The horizontal dashed lines are the values of the Strouhal numbers, $St_y = 0.121$ and $St_z = 0.175$ of the reference case. The vertical dashed lines mark the C_q^{Opt} value for which the mean base drag C_B is minimum.

500 (b). However the relative locations of the probes to the spatial envelop of the fluctuations,
 501 do not allow for a direct deduction between Fig. 11 and Fig. 16 (b), as it was the case
 502 between Fig. 8 and Fig. 16 (a) for the L configuration.

503 3.5. Leakage of the recirculating region

504 The experimental implementations do not allow for the tracking of the injected mass
 505 but the injected momentum can be assessed by looking at the difference between the mean
 506 velocity modulus at a given blowing rate with that of $C_q = 0$, say $\Delta U_{xy}^{*i} = U_{xy}^{*i} - U_{xy0}^{*i}$
 507 in the $z = 0$ plane and $\Delta U_{xz}^* = U_{xz}^* - U_{xz0}^*$ in the $y = 0$ plane where $i = P$ or N denotes the
 508 state. Both cases will be referred to as mean momentum modifications. We superimpose to
 509 the mean flow streamlines in Fig. 17 the mean momentum modification when blowing in
 510 the LR configuration. We only display the optimal C_q^{Opt} (Fig. 17a) and maximal injection
 511 $C_q = 0.0185$ (Fig. 17b) corresponding to the extreme cases of respectively low and high

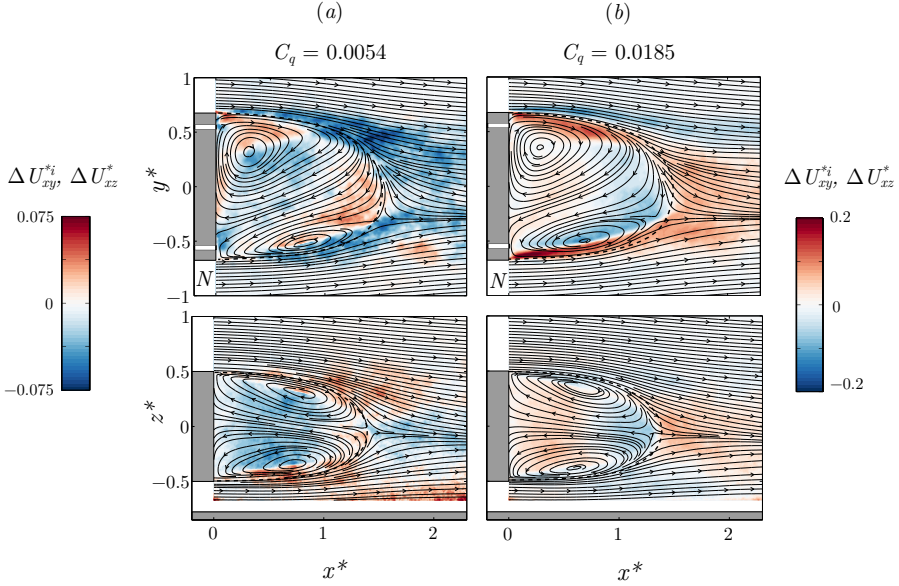


Figure 17: Blowing in LR configuration. Mean momentum modification superimposed to the mean streamlines for (a) $C_q = C_q^{\text{Opt}}$ and (b) maximum injection $C_q = 0.0185$. (a,top) $\Delta U_{xy}^{*i} = U_{xy}^{*i} - U_{xy0}^{*i}$, (b,bottom) $\Delta U_{xz}^* = U_{xz}^* - U_{xz0}^*$, $i = P$ or N denotes the state. The dashed curve represents the separatrix of the recirculating bubble with no injection.

512 base drag. The blowing jets are not distinguishable in the mass regime (Fig. 17a,top), but
 513 a momentum reduction is clearly visible outside the bubble. It is an indication that the
 514 bubble is sweating low momentum by leaking the continuous injection mass. The bubble
 515 size is slightly increased when compared to the dashed curve representing the separatrix
 516 obtained with no injection. For the maximum injection coefficient in Fig. 17(b,top), the
 517 bubble size is decreased, the momentum is significantly increased at the slits exit inside
 518 the bubble. There are also indications of leakage shown by the momentum decrease just
 519 outside the bubble at the right hand side injection and momentum increases aft the
 520 bubble closure (also observable in the perpendicular plane in Fig. 17b,bottom). In both
 521 cases, it reveals that momentum from the bubble has mixed with the flow outside the
 522 bubble and then been naturally transported downstream: at the right outer edge with
 523 high speed flow and in the wake with low speed flow.

524 The evacuation of the injected mass by the wake is also observable in Fig. 18 for TB
 525 configuration. The optimal blowing is associated with an overall momentum reduction
 526 outside the bubble in Fig. 18(a) and the maximal blowing to momentum increase aft the
 527 bubble in Fig. 18(b,top). The leakage pattern in the momentum regime is dominant in
 528 the plane $z = 0$ and very different to the LR configuration observed in Fig. 17(b,top).
 529 The optimal blowing at $C_q = 0.0078$ also produces a larger bubble size (Fig. 18a) and
 530 the maximal blowing a smaller bubble size (Fig. 18b).

531 Similar results are obtained for all other configurations, whose main differences lay
 532 only in the leakage pattern of the momentum regime. As a conclusion, the path of the
 533 injected flow is never detectable in the mean flow displayed with streamlines as ideally
 534 sketched in Bearman (1967) in the theoretical case of a steady wake but mixed and then
 535 evacuated in the wake through the unsteady dynamics of the shear layers and bubble
 536 closure.

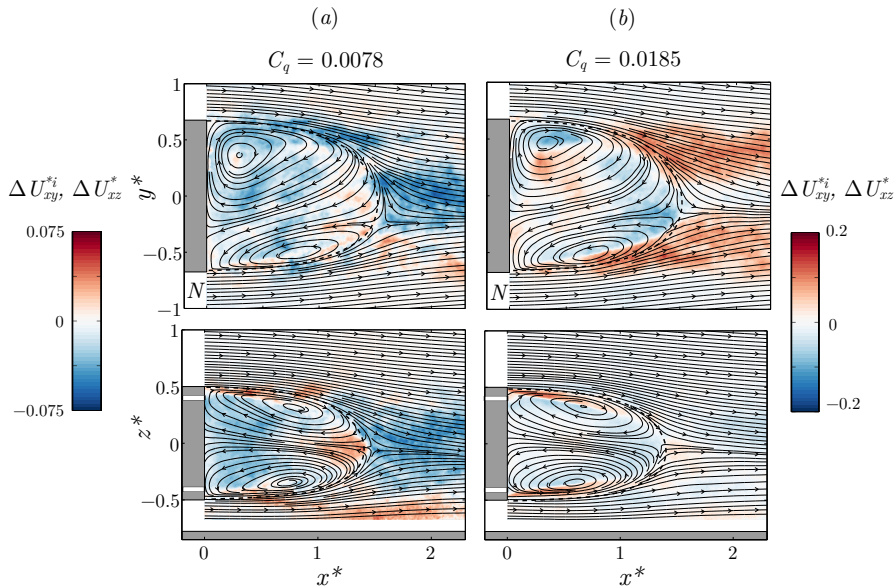


Figure 18: Blowing in TB configuration. Mean momentum modification superimposed to the mean streamlines for (a) $C_q = C_q^{\text{Opt}}$ and (b) maximum injection $C_q = 0.0185$. (a,top) $\Delta U_{xy}^{*i} = U_{xy}^{*i} - U_{xy0}^{*i}$, (b,bottom) $\Delta U_{xz}^* = U_{xz}^* - U_{xz0}^*$, $i = P$ or N denotes the state. The dashed curve represents the separatrix of the recirculating bubble with no injection.

537

3.6. Drag and recirculation length

538

539

540

541

542

543

544

545

546

547

548

549

550

551

552

553

554

555

556

557

558

559

The base drag coefficient variation versus the drag coefficient variation in Fig. 19(a) deviates slightly from the linear law of slope 1. This linear law is expected for a blunt base geometry when pressure drag is the only source of drag. However, the slope of 1 is satisfactorily achieved for the mass regime which concerns all the data points from zero to the optimal values of lower drag (Fig. 19a, inset). A significant curvature is observed when the blowing is further increased above the optimal values (momentum regime) leading to drag increase. This effect is likely to be due to the non-linear interaction of the blowing jet with the flow at the base that cannot be assessed in the simple expression of thrust and slit head loss removals as used in (2.6). The plot also points out the good accuracy of the base drag estimation using the four pressure taps, indicating that it is an effective way to access the main characteristics of the base pressure distribution for this geometry.

The bubble recirculating length is correlated to the base drag as can be seen in Fig. 19(b). The larger the bubble the smaller the base drag and vice versa. It also indicates that increasing blowing in the mass regime (resp. momentum regime) increases (resp. decreases) the recirculating length. This relationship is illustrated by the results shown in both Fig. 17 and Fig. 18 displaying the shape of the recirculating bubble for lowest (a) and highest (b) base drag of two blowing configurations. The relation between separation length and base drag is a classical result for blunt base bluff bodies, either two-dimensional (Bearman 1967), axisymmetric (Mariotti *et al.* 2015) or three-dimensional (Grandemange *et al.* 2013b). The small variations compared to the non-blowing value produce the affine relationship as observed in Fig. 19(b):

$$C_B = C_{B0} - 0.185(L_r^* - L_{r0}^*). \quad (3.1)$$

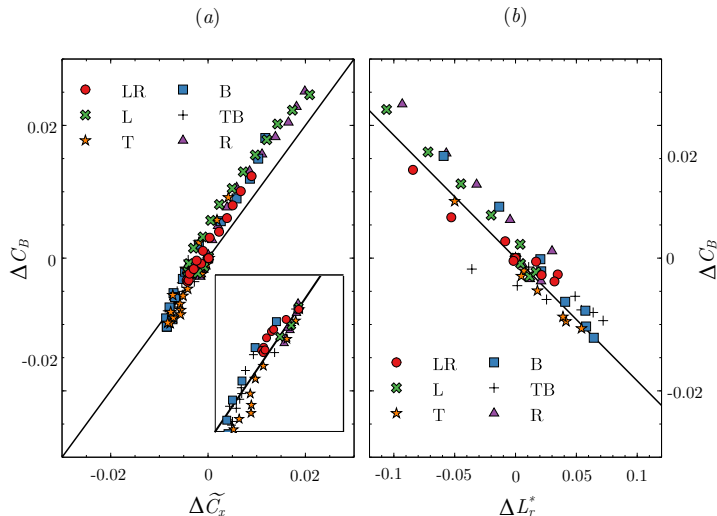


Figure 19: Base drag coefficient vs. drag coefficient (a) and recirculating bubble length (b). The subscript 0 denotes values obtain with $C_q = 0$. In (a), continuous line is $\Delta C_B = \Delta \tilde{C}_x$ and the inlet is a close-up view of the plot showing data in mass regime only. In (b), continuous line is $\Delta C_B = -0.185 \Delta L_r^*$.

560 The aim of Eq. (3.1) is to highlight the relation between C_B and L_r^* when a steady per-
 561 metric blowing (of small momentum) is injected through the base of a three-dimensional
 562 blunt body. The correlation may depend on the body geometry and flow conditions.
 563 Therefore, we cannot ensure that such dependence is universal, and a different value of
 564 the slope and power law may be found in different configurations.

565 4. Discussion

566 4.1. Wake modes sensitivity to local blowing

567 The sensitivity of the static mode to the local base blowing is summarized in Fig. 12
 568 for all the asymmetric configurations of blowing and Fig. 15 for all the symmetric ones.
 569 The static mode strength is weakened by the blowing during the mass regime (empty
 570 symbols) with a maximum reduction of 10% to 20% depending on the configuration.
 571 Figure 20(a,b) shows the correlation of the base drag variation with the base pressure
 572 gradient modulus. Whatever the configuration, there is a well defined correlation in the
 573 mass regime as shown in Fig. 20(a) indicating that base drag reduction is associated with
 574 permanent asymmetry reduction. In the momentum regime, the plot in Figure 20(b) is
 575 more scattered with different configurations indicating no straightforward relationship
 576 between asymmetry and drag. We can actually distinguish two behaviors. For the LR
 577 and TB symmetric configurations for which the wake is always bistable, the base drag is
 578 increased keeping constant the asymmetry strength. For the asymmetric configurations
 579 L, R, T and B, the base drag increase is associated with asymmetry strength increase.
 580 We believe these effects to be a simple consequence of the symmetry properties of the
 581 blowing configuration where only asymmetric configurations are capable to amplify the
 582 wake asymmetry.

583 Static mode orientation, given by the orientation of the base pressure gradient of
 584 the state, is found to be sensitive to local blowing. For all asymmetric configurations

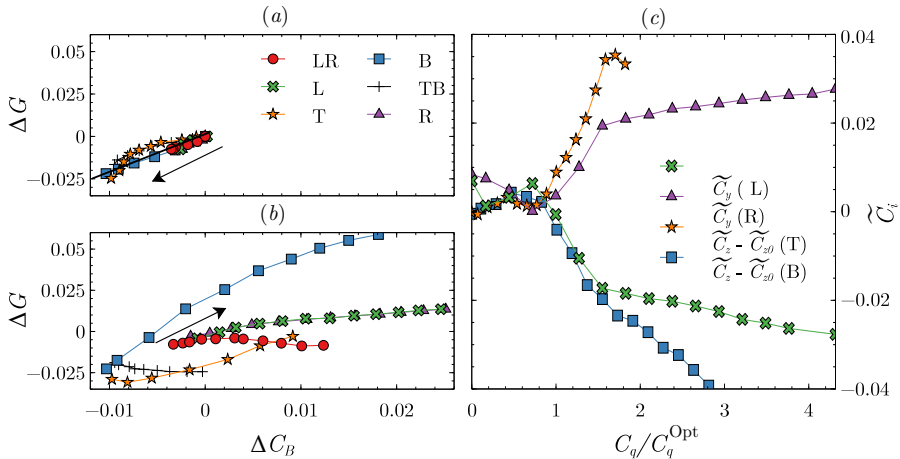


Figure 20: Variation of base pressure gradient modulus $\Delta G = G - G_0$ in the mass (a) and momentum (b) regimes vs. base drag variation $\Delta C_B = C_B - C_{B0}$ for all configurations. In (a,b) the arrows indicate the direction of blowing coefficient C_q increase. Lateral force coefficients (c) vs. the reduced blowing coefficient C_q/C_q^{Opt} for asymmetric slits configurations.

585 in the momentum regime, blowing is able to impose the mode orientation as can be
 586 seen in Fig. 12. While L or R configuration corresponds to state selection, the T and B
 587 configurations force a non-trivial rotation of the static mode. Similar static mode rotation
 588 was observed by introducing steady disturbances breaking the top/bottom symmetry of the
 589 rectangular base either obtained by small obstructions (Barros *et al.* 2017) or by
 590 pitching the body (Bonnaivon & Cadot 2018). The orientation sensitivity of the static
 591 mode has a large impact on the aerodynamic force as shown in Fig. 20. In Bonnaivon &
 592 Cadot (2018) the lateral force produced by the P and N state is shown to be $C_i = \pm 0.02$
 593 ($i = y, z$ denotes the direction of the instability). Thus for $C_q = 1.5 C_q^{\text{Opt}}$ in Fig. 20(c),
 594 the lateral force is mostly produced by the strength of the re-orientated static mode
 595 rather than by the jet itself.

596 As characterized in Grandemange *et al.* (2013a), the spatial envelopes of the low and
 597 high frequency modes are intimately related to the static mode orientation. Since we
 598 do not observe any significant changes in the two frequency values independently to the
 599 jet intensity and mode orientation in the analysis presented in Fig. 16, it is likely that
 600 the periodic modes sensitivity is essentially explained by the static mode orientation
 601 sensitivity to the blowing.

602 4.2. Base drag modification

603 4.2.1. Model

604 We propose a simple mechanism for the base drag variation aiming at understanding
 605 the complexity of the Fig. 7. The starting point is the well established relationship
 606 between the mean bubble recirculation length and base drag for this type of geometry
 607 (Grandemange *et al.* 2013b). The correlation is supported by the inviscid cavity models
 608 (Wu 1972) that establish a general behavior of base pressure evolving as positive power
 609 laws of the inverse of the cavity length. Physically, the low base pressure is produced by
 610 the flow curvature around the cavity. For viscous wake flows at large Reynolds number,
 611 this trend still remains with the recirculating bubble playing the role of the cavity (Roshko

1993). In our case, the variations of the bubble length L_r reported in Fig. 19(b) are small compared to the reference value of $L_r^{\text{Ref}} = 1.45$ which linearizes the power law to the approximation (3.1).

We follow now the mechanism proposed by Gerrard (1966) for the adjustment of the recirculating bubble length behind a bluff body. It results from the equilibrium of fluxes filling and emptying the recirculating region. For the natural case, the growth rate of the free shear layers is associated with velocity entrainment along the shear layer, feeding the shear layer by emptying the recirculating region. This total volumetric flux is denoted by b in Fig. 21. The key point is that this flux depends on the free shear layer length, and thus increases as L_r increases and decreases as L_r decreases. The intense unsteady activity at the bubble closure such as Kelvin-Helmholtz like instabilities produces rolls-up allowing a feedback flux c to fill the recirculating region together with a fluid engulfment with flux a in the shed vortice (see sketch in Fig. 21. Momentum of flux c is strongly reduced by dissipation. Fluxes a and b are dominated by the inviscid dynamics of the roll-up. The equilibrium of fluxes is $a + b = c$. In our case, the mixing layer should be considered as turbulent, known to have a constant growth rate (Champagne *et al.* 1976; Pope 2000), equivalent to a constant entrainment velocity $V_E = V_E^* U_\infty$ along the shear layers. The flux entrained by the mixing layers delimiting the whole separated region is estimated to $b = V_E \ell L_r$, where ℓ is the peripheral length of the mixing layers (i.e : $\ell = 2(h + w)$ for our geometry). The equilibrium for the natural case gives $a + V_E \ell L_{r0} = c$, where L_{r0} is the natural bubble length (i.e. without blowing).

The mass regime is characterized by an external flux that feeds the recirculating region but whose momentum is dissipated. Compared to the natural scenario described above, we only need to take into account the additional flow rate source $q = q_b$ to c . The mass regime equilibrium illustrated in Fig. 21 leads to $a + V_E \ell L_r = c + q_b$. As momentum of flux q_b is dissipated, we should not expect any significant modifications of the flow, and so for fluxes a and c from the natural case. Hence the flow rate budget gives :

$$L_r = L_{r0} + \frac{q_b}{V_E \ell}. \quad (4.1)$$

For this mass regime, the recirculation length increases as the injection flux q_b increases with a slope depending on the mean entrainment velocity of the extended shear layers length. This can be pictured as the inflation of the recirculating bubble by the base blowing flux, thus increasing shear layers length and flux leaking through the shear layers, until these two fluxes compensate. The leaking is evidenced with the observation of low momentum sweating in the results section §3.5.

On the other hand, the momentum regime is characterized by a deflating of the recirculating bubble with a reduction of the recirculating length as base blowing is increased (see §3.6). On the contrary to the mass regime, the momentum of the blowing flux strongly modifies the flow by entirely evacuating the flux q_b through the shear together with increasing the shear layers entrainment velocity. This modification would be responsible for emptying the recirculating region, i.e. no injection in the recirculating region, $q = 0$ and increase of flux b that would re-adjust the bubble length (see the sketch of the momentum regime is Fig. 21). To retrieve the observed effect, the flux entrained by the shear layers must be a combination of disturbed and undisturbed free shear layers, $b = (\alpha_1 U_\infty + \alpha_2 U_b) \ell L_r$, and that the contributions of a and c are constant. The flow rate budget $a + (\alpha_1 U_\infty + \alpha_2 U_b) \ell L_r = c$ leads to :

$$L_r = \frac{L_{r1}}{1 + \frac{\alpha_2}{\alpha_1} \frac{U_b}{U_\infty}} \approx L_{r1} \left(1 - \frac{\alpha_2}{\alpha_1} \frac{U_b}{U_\infty} \right), \quad (4.2)$$

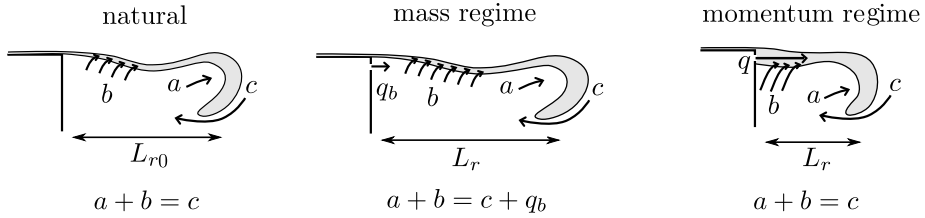


Figure 21: Conceptual sketch illustrating the flow rate budget between filling and emptying of the separated region (see text) for the natural wake, low flow rate injection (mass regime) and large flow rate injection (momentum regime). Grey contours depict the free shear layer that develops from the separation. At further stage of the unsteady dynamics, the shear layer roll-up produces a detached vortex that evacuates downstream fluxes b and a from the separated region.

656 Non-dimensional expressions for (4.1) and (4.2) are :

$$L_r^* = L_{r0}^* + \frac{w}{V_E^* \ell} C_q, \quad L_r^* = L_{r1}^* \left(1 - \frac{\alpha_2}{\alpha_1} C_u\right), \quad (4.3)$$

657

658 4.2.2. Mass regime

659 The values of V_E^* displayed in table 4 are computed from (4.3) using the correlation
 660 (3.1) providing $\frac{\partial C_B^*}{\partial C_q} = -0.185 L_r^*$ and the measured slope $\frac{\partial C_B}{\partial C_q}|_0$ in table 3:

$$V_E^* = -0.185 \frac{w}{\frac{\partial C_B}{\partial C_q}|_0 \ell}, \quad (4.4)$$

661 Classical measurements in mixing layers (Champagne *et al.* 1976; Dimotakis 1991; Pope
 662 2000) report the parameter S , defined as $S = \frac{U_C}{U_S} \frac{d\delta}{dx}$ where U_C is the mean shear velocity,
 663 U_S the velocity jump and $\frac{d\delta}{dx}$ the growth rate of the mixing layer. In our case $U_S = U_\infty$ for
 664 which a simple flow rate budget gives $V_E dx = U_C d\delta$, thus $S = V_E^*$. The range of reported
 665 values is from $S \approx 0.06$ to $S \approx 0.11$ for undisturbed mixing layers (Dimotakis 1991).
 666 This wide range is related to high sensitivities to the initial condition of the mixing layer
 667 at separation. The values we obtained for V_E^* in table 4 match satisfactorily this range
 668 indicating that the budget volumetric model is plausible to explain the drag reduction
 669 in the mass regime. The assumption that injected momentum does not modify the flow
 670 dynamics in the mass regime, implies an independence of the bubble growth with the
 671 blowing location. It is actually almost the case for the L, R and LR configurations for
 672 which the V_E^* values are in the range 0.059–0.075. It is even better shown by the identical
 673 slopes in Fig. 9(b) whether injection occurs in the adverse flow region (Fig. 9d,top) or
 674 reversed flow region (Fig. 9d,bottom) of the separated bubble. For these 3 configurations,
 675 flow characteristics given in table 1 are almost identical. This is not the case for the T
 676 and B configurations indicating significant changes in the vertical base pressure gradient
 677 component. Hence, one can argue than the free shear properties, and then the V_E^* values
 678 can change from one configuration to the other due to an influence of the slit on the
 679 initial condition of the free shear layers development.

Configuration	L	R	T	B	LR	TB
V_E^*	0.075	0.074	0.055	0.036	0.059	0.039
α_2/α_1	0.127	0.127	0.235	0.237	0.174	0.180

Table 4: Parameters (see text) of the flow rate budget model for the mass (4.1) and momentum (4.2) regimes for all blowing configurations.

4.2.3. Momentum regime

The ratio α_2/α_1 can also be estimated using again the correlation (3.1) in (4.3) providing

$$C_B - C_{B0} = -0.185(L_{r1}^* - L_{r0}^*) + 0.185L_{r1}^* \frac{\alpha_2}{\alpha_1} C_u \quad (4.5)$$

and the linear regression obtained in the momentum regime displayed in table 3. Values for α_2/α_1 are displayed in table 4. The ratio is a measurement of the efficiency of the perturbed shear layers by the momentum injection to evacuate fluid from the recirculating region. We can see in table 4 a wide variation of the ratio, and the basic expectation of having twice the value of the single slit configurations for the double slits configurations is not at all respected.

The smallest value of α_2/α_1 is obtained for the L or R blowing, for which the corresponding forced flow is shown in Fig. 8(c). The largest ratio is obtained in either the T or B configurations, for which the forced flow is shown in Fig. 11(c). For all of these single slit configurations, the jet is blowing in an adverse flow region of the static mode, at the outer edge of the steady vortex. The main difference between the lateral and top/bottom blowing is that the global rotation of the static mode has inverted the base aspect ratio of the recirculating region. It is likely that the difference in the wake base aspect ratio is the cause for the discrepancies in the shear ratio values α_2/α_1 .

Intermediate values are found for the symmetric configurations for which bistability persists, and where the static mode still remains orientated in the horizontal direction (Fig. 14a). For the case of the TB configuration, the blowing is never located at the outer edge of the steady vortex as for the single T injection (Fig. 11c), but in the highly fluctuating shear layers as shown in Fig. 14(c), likely to be much less efficient to evacuate fluid from the recirculation region. For the LR configuration (Fig. 13c), there is one blowing slit located at the outer edge of the steady vortex as for the single L or R injection (Fig. 8c), while the other slit blows in the reversed flow region at the proximity of a highly fluctuating shear layer. This permanent asymmetry plausibly explains why the value of α_2/α_1 for the LR configuration is lower than twice that of the L or R configuration.

4.3. Critical blowing of the transition

If the transition defined by the minimum base drag value is determined by a critical parameter associated with each slit, we would expect the critical parameter for the TB configuration to be the mean of the critical parameters obtained for T and B transition. This is not true if the parameter is the momentum coefficient C_u as can be seen in Fig. 7(b). It is then unlikely that the momentum coefficient C_u could be the critical parameter for the transition between the mass and the momentum regime. However, by looking at the C_q -plot in Fig. 7(a), the transition value for the TB configuration $C_q^{\text{Opt}} = 7.8 \times 10^{-3}$ is comprised within the two transition values $C_q^{\text{Opt}} = 10.2 \times 10^{-3}$ of the T configuration and $C_q^{\text{Opt}} = 6.6 \times 10^{-3}$ of the B configuration and matches

718 approximately the average value. For LR configuration, the flow is always bistable, which
 719 means that during the random switching dynamics between the P and N state, one
 720 slit is permanently injecting in the adverse flow region while the other is permanently
 721 injecting in the reversed flow region (see Fig. 13). For consistency with the T, B and
 722 TB configurations discussed above, we would expect that the LR transition value should
 723 match the average of the transition values for a single injection in the reversed flow region
 724 and a single injection in the adverse flow region. These two transition values are given
 725 for the wake either locked in a P state or a N state with a single slit injection. It is
 726 exactly the case studied in Fig. 9 in the R blowing configuration. The transition for the
 727 N state occurs at $C_q^{\text{Opt}} = 4.3 \times 10^{-3}$ while for the P state $C_q^{\text{Opt}} = 6.6 \times 10^{-3}$. The
 728 transition value $C_q^{\text{Opt}} = 5.5 \times 10^{-3}$ of the LR configuration is then also comprised within
 729 the two single cases and approximately corresponds to their average. This consistency
 730 between the configurations in the C_q -plot and the discrepancy in the C_u -plot shows that
 731 the transition between the mass and the momentum regime is governed by a critical
 732 value of the global injected flow rate (also depending on the location of the injection)
 733 and not to the mean momentum of the base blowing. It seems contradictory to results
 734 of Wood (1964) and may emphasize differences whether the flow is 2D with injection in
 735 the middle of the base (Wood 1964) or 3D with injections at the proximity of the shear
 736 layers (the present study).

737 Finally, to extend the mass regime and then to increase the base drag reduction it is
 738 favourable to inject in a reversed flow region of the recirculating bubble (see Figs. 9 and
 739 10). It is likely that the injected jet momentum dissipation is enhanced in this case.

740 5. Conclusion

741 It is known that, in two-dimensional bodies the bleed has a stabilising effect on
 742 the global instability and von-Karman vortex shedding can be substantially weakened
 743 resulting in a large drag reduction. However, in three-dimensional bluff bodies of interest
 744 in the present work, shear instabilities are still present but their contribution to drag is
 745 weaker and the resulting effects of bleed on the near wake flow are mainly related to the
 746 manipulation and control of the static modes.

747 In particular, there are two very distinctive sensitivities of three-dimensional wake
 748 modes to local base blowing whether blowing is in the mass or momentum regime. The
 749 mass regime shows almost no dependency on the injection location, it is accompanied
 750 with the recirculating bubble inflating producing the drag reduction. In addition to
 751 these observations that are common to two-dimensional bluff bodies, it is found in this
 752 work that the mass regime is characterized by a reduction of the static asymmetric
 753 mode strength. The flow makes a transition to the momentum regime for a critical
 754 flow rate depending on the injection location. The momentum regime is found to be
 755 mainly governed by the interaction with the static asymmetric mode, either selecting a
 756 pre-existing state or forcing a rotation of the static mode orientation. This interaction
 757 leads to drastic changes of the recirculating bubble topology while the periodic modes
 758 shapes are found to follow the modification of the static mode orientation. Compared to
 759 two-dimensional bluff bodies, the interaction lead to non-trivial base drag variation with
 760 blowing location and intensity. There is no straightforward correlation with the static
 761 mode strength, but globally, the momentum regime is associated with a recirculating
 762 bubble deflating together with a drag increase. The experimental results are used to
 763 build a flow rate budget model of the recirculating region taking into account shear
 764 layers modification for the momentum regime. The work offers an experimental data
 765 basis with comprehensive interaction of base blowing with the three-dimensional wake

766 and its main modes. It could be used in the future for flow control in the presence of a
 767 static asymmetric wake mode.

768

769 The authors are grateful to Peter Bearman for useful discussions and the critical
 770 reading of the manuscript. This work has been partially supported by the Spanish
 771 MINECO and European Funds under projects DPI2017-89746- R and DPI2017-88201-
 772 C3-2-R. Moreover, J.I.J.G. and M.L.D want to thank the Spanish MECD for the fi-
 773 nancial support provided under José Castillejo grant CAS18/00379 and Fellowship FPU
 774 014/02945 respectively.

REFERENCES

- 775 AHMED, S. R., RAMM, G. & FALTIN, G. 1984 Some salient features of the time-averaged ground
 776 vehicle wake. In *SAE Technical Paper*, , vol. 840300.
- 777 APELT, C. J. & WEST, G. S. 1975 The effects of wake splitter plates on bluff body flow in the
 778 range $10^4 < Re < 5 \times 10^4$. Part 2. *Journal of Fluid Mechanics* **71** (01), 145–160.
- 779 BARROS, D., BORÉE, J., CADOT, O., SPOHN, A. & NOACK, B. R. 2017 Forcing symmetry
 780 exchanges and flow reversals in turbulent wakes. *Journal of Fluid Mechanics* **829**, R1.
- 781 BARROS, D., BORÉE, J., NOACK, B. R. & SPOHN, A. 2016a Resonances in the forced turbulent
 782 wake past a 3D blunt body. *Physics of Fluids* **28** (6), 065104.
- 783 BARROS, D., BORÉE, J., NOACK, B. R., SPOHN, A. & RUIZ, T. 2016b Bluff body drag
 784 manipulation using pulsed jets and Coanda effect. *Journal of Fluid Mechanics* **805**, 422–
 785 459.
- 786 BEARMAN, P. W. 1967 The effect of base bleed on the flow behind a two-dimensional model
 787 with a blunt trailing edge. *The Aeronautical Quarterly* **18** (3), 207–224.
- 788 BOHORQUEZ, P., SANMIGUEL-ROJAS, E., SEVILLA, A., JIMÉNEZ-GONZÁLEZ, J. I. & MARTÍNEZ-
 789 BAZÁN, C. 2011 Stability and dynamics of the laminar wake past a slender blunt-based
 790 axisymmetric body. *Journal of Fluid Mechanics* **676**, 110–144.
- 791 BONNAVION, G. & CADOT, O. 2018 Unstable wake dynamics of rectangular flat-backed bluff
 792 bodies with inclination and ground proximity. *Journal of Fluid Mechanics* **854**, 196–232.
- 793 BONNAVION, G. & CADOT, O. 2019 Boat-tail effects on the global wake dynamics of a flat-
 794 backed body with rectangular section. *Journal of Fluids and Structures* **89**, 61–71.
- 795 BRACKSTON, R. D., GARCÍA DE LA CRUZ, J. M., WYNN, A., RIGAS, G. & MORRISON, J. F.
 796 2016 Stochastic modelling and feedback control of bistability in a turbulent bluff body
 797 wake. *Journal of Fluid Mechanics* **802**, 726–749.
- 798 BRACKSTON, R. D., WYNN, A. & MORRISON, J. F. 2018 Modelling and feedback control of
 799 vortex shedding for drag reduction of a turbulent bluff body wake. *International Journal*
 800 *of Heat and Fluid Flow* **71**, 127–136.
- 801 CADOT, O., EVRARD, A. & PASTUR, L. 2015 Imperfect supercritical bifurcation in a three-
 802 dimensional turbulent wake. *Physical Review E* **91** (6).
- 803 CHAMPAGNE, F. H., PAO, Y. H. & WYGNANSKI, I. J. 1976 On the two-dimensional mixing
 804 region. *Journal of Fluid Mechanics* **74** (02), 209–250.
- 805 GARCÍA DE LA CRUZ, J. M., BRACKSTON, R. D. & MORRISON, J. F. 2017 Adaptive base-flaps
 806 under variable cross-wind. *SAE Technical Paper* **2017-01-7000**.
- 807 GARCÍA DE LA CRUZ, J. M., OXLADE, A. R. & MORRISON, J. F. 2017 Passive control of base
 808 pressure on an axisymmetric blunt body using a perimetric slit. *Physical Review Fluids*
 809 **2** (4), 043905.
- 810 DALLA LONGA, L., EVSTAFYEVA, O. & MORGANS, A. S. 2019 Simulations of the bi-modal wake
 811 past three-dimensional blunt bluff bodies. *Journal of Fluid Mechanics* **866**, 791–809.
- 812 DIMOTAKIS, P. E. 1991 Turbulent free shear layer mixing and combustion. *High Speed Flight*
 813 *Propulsion Systems* pp. 265–340.
- 814 EVRARD, A., CADOT, O., HERBERT, V., RICOT, D., VIGNERON, R. & DÉLERY, J. 2016 Fluid
 815 force and symmetry breaking modes of a 3D bluff body with a base cavity. *Journal of*
 816 *Fluids and Structures* **61**, 99–114.

- 817 FABRE, D., AUGUSTE, F. & MAGNAUDET, J. 2008 Bifurcations and symmetry breaking in the
818 wake of axisymmetric bodies. *Physics of Fluids* **20**, 051702.
- 819 GERRARD, J. H. 1966 The mechanics of the formation region of vortices behind bluff bodies.
820 *Journal of Fluid Mechanics* **25** (2), 401–413.
- 821 GRANDEMANGE, M., CADOT, O. & GOHLKE, M. 2012 Reflectional symmetry breaking of the
822 separated flow over three-dimensional bluff bodies. *Physical Review E* **86** (3), 035302.
- 823 GRANDEMANGE, M., GOHLKE, M. & CADOT, O. 2013a Bi-stability in the turbulent wake past
824 parallelepiped bodies with various aspect ratios and wall effects. *Physics of Fluids* **25** (9),
825 095103.
- 826 GRANDEMANGE, M., GOHLKE, M. & CADOT, O. 2013b Turbulent wake past a three-dimensional
827 blunt body. Part 1. global modes and bi-stability. *Journal of Fluid Mechanics* **722**, 51–84.
- 828 GRANDEMANGE, M., GOHLKE, M. & CADOT, O. 2014 Turbulent wake past a three-dimensional
829 blunt body. Part 2. Experimental sensitivity analysis. *Journal of Fluid Mechanics* **752**,
830 439–461.
- 831 GREENBLATT, D. & WYGNANSKI, I. J. 2000 The control of flow separation by periodic
832 excitation. *Progress in Aerospace Sciences* **36** (7), 487–545.
- 833 JIMÉNEZ-GONZÁLEZ, J. I., SANMIGUEL-ROJAS, E., SEVILLA, A. & MARTÍNEZ-BAZÁN, C. 2013
834 Laminar flow past a spinning bullet-shaped body at moderate angular velocities. *Journal*
835 *of Fluids and Structures* **43**, 200–219.
- 836 JIMÉNEZ-GONZÁLEZ, J. I., SEVILLA, A., SANMIGUEL-ROJAS, E. & MARTÍNEZ-BAZÁN, C. 2014
837 Global stability analysis of the axisymmetric wake past a spinning bullet-shaped body.
838 *Journal of Fluid Mechanics* **748**, 302–327.
- 839 KIYA, M. & ABE, Y. 1999 Turbulent elliptic wakes. *Journal of Fluids and Structures* **13** (7-8),
840 1041–1067.
- 841 LI, R., BARROS, D., BORÉE, J., CADOT, O., NOACK, B. R. & CORDIER, L. 2016 Feedback
842 control of bimodal wake dynamics. *Experiments in Fluids* **57** (10), 158.
- 843 LITTLEWOOD, R. P. & PASSMORE, M. A. 2012 Aerodynamic drag reduction of a simplified
844 squareback vehicle using steady blowing. *Experiments in Fluids* **53** (2), 519–529.
- 845 LUCAS, J. M., CADOT, O., HERBERT, V., PARPAIS, S. & DÉLERY, J. 2017 A numerical
846 investigation of the asymmetric wake mode of a squareback Ahmed body - effect of a
847 base cavity. *Journal of Fluid Mechanics* **831**, 675–697.
- 848 MARIOTTI, A., BURESTI, G. & SALVETTI, M. V. 2015 Connection between base drag, separating
849 boundary layer characteristics and wake mean recirculation length of an axisymmetric
850 blunt-based body. *Journal of Fluids and Structures* **55**, 191–203.
- 851 PASQUETTI, R. & PERES, N. 2015 A penalty model of synthetic micro-jet actuator with
852 application to the control of wake flows. *Computers & Fluids* **114** (0), 203–217.
- 853 PAVIA, G., PASSMORE, M. & GAYLARD, A. 2016 Influence of short rear end tapers on the
854 unsteady base pressure of a simplified ground vehicle. *SAE Technical Paper* **2016-01-**
855 **1590**.
- 856 PERRY, A., PASSMORE, M. A. & FINNEY, A. 2015 Influence of short rear end tapers on the base
857 pressure of a simplified vehicle. *SAE International Journal of Passenger Cars—Mechanical*
858 *Systems* **8** (1).
- 859 POPE, S. B. 2000 *Turbulent flows*. Cambridge University Press.
- 860 RIGAS, G., MORGANS, A. S., BRACKSTON, R. D. & MORRISON, J. F. 2015 Diffusive dynamics
861 and stochastic models of turbulent axisymmetric wakes. *Journal of Fluid Mechanics* **778**,
862 R2.
- 863 RIGAS, G., OXLADE, A. R., MORGANS, A. S. & MORRISON, J. F. 2014 Low-dimensional
864 dynamics of a turbulent axisymmetric wake. *Journal of Fluid Mechanics* **755**, R5.
- 865 ROSHKO, A. 1993 Perspectives on bluff body aerodynamics. *Journal of Wind Engineering and*
866 *Industrial Aerodynamics* **49** (1-3), 79–100.
- 867 ROUMÉAS, M., GILLIÉRON, P. & KOURTA, A. 2009 Analysis and control of the near-wake flow
868 over a square-back geometry. *Computers and Fluids* **38** (1), 60–70.
- 869 SAKAMOTO, H. & HANIU, H. 1990 A study on vortex shedding from spheres in a uniform flow.
870 *Journal of Fluids Engineering* **112**, 386–392.
- 871 SANMIGUEL-ROJAS, E., SEVILLA, A., MARTÍNEZ-BAZÁN, C. & CHOMAZ, J. M. 2009 Global
872 mode analysis of axisymmetric bluff-body wakes: Stabilization by base bleed. *Physics of*
873 *Fluids* **21** (11), 114102.

- 874 SEVILLA, A. & MARTÍNEZ-BAZÁN, C. 2004 Vortex shedding in high Reynolds number
875 axisymmetric bluff-body wakes: local linear instability and global bleed control. *Physics*
876 *of Fluids* **16** (9), 3460–3469.
- 877 TANNER, M. 1975 Reduction of base drag. *Progress in Aerospace Sciences* **16** (4), 369–384.
- 878 VARON, E., EULALIE, Y., EDWIGE, S., GILOTTE, P. & AIDER, J. L. 2017 Chaotic dynamics
879 of large-scale structures in a turbulent wake. *Physical Review Fluids* **2**, 034604.
- 880 VISWANATH, P. R. 1996 Flow management techniques for base and afterbody drag reduction.
881 *Progress in Aerospace Sciences* **32** (2), 79–129.
- 882 VOLPE, R., DEVINANT, P. & KOURTA, A. 2015 Experimental characterization of the unsteady
883 natural wake of the full-scale square back Ahmed body: flow bi-stability and spectral
884 analysis. *Experiments in Fluids* **56** (5).
- 885 WASSEN, E., EICHINGER, S. & THIELE, F. 2010 Simulation of active drag reduction for a
886 squareback vehicle. *Active Flow Control II* pp. 241–255.
- 887 WONG, D. T. M. & MAIR, W. A. 1983 Boat-tailed afterbodies of square section as drag-
888 reduction devices. *Journal of Wind Engineering and Industrial Aerodynamics* **12** (2),
889 229–235.
- 890 WOOD, C. J. 1964 The effect of base bleed on a periodic wake. *The Aeronautical Journal*
891 **68** (643), 477–482.
- 892 WU, T. Y. T. 1972 Cavity and wake flows. *Annual Review of Fluid Mechanics* **4** (1), 243–284.